

# Theory and simulation of the confined Lebwohl-Lasher model

R. G. Marguta

*Instituto de Química-Física Rocasolano, CSIC, Serrano 119, E-28006 Madrid, Spain*

Y. Martínez-Ratón

*Grupo Interdisciplinar de Sistemas Complejos (GISC), Departamento de Matemáticas, Escuela Politécnica Superior, Universidad Carlos III de Madrid, Avenida de la Universidad 30, E-28911 Leganés, Madrid, Spain*

N. G. Almarza

*Instituto de Química-Física Rocasolano, CSIC, Serrano 119, E-28006 Madrid, Spain*

E. Velasco

*Departamento de Física Teórica de la Materia Condensada and Instituto de Ciencia de Materiales Nicolás Cabrera, Universidad Autónoma de Madrid, E-28049 Madrid, Spain*

(Received 1 July 2010; revised manuscript received 29 January 2011; published 5 April 2011)

We discuss the Lebwohl-Lasher model of nematic liquid crystals in a confined geometry, using Monte Carlo simulation and mean-field theory. A film of material is sandwiched between two planar, parallel plates that couple to the adjacent spins via a surface strength  $\epsilon_s$ . We consider the cases where the favored alignments at the two walls are the same (symmetric cell) or different (asymmetric cell). In the latter case, we demonstrate the existence of a *single* phase transition in the slab for all values of the cell thickness. This transition has been observed before in the regime of narrow cells, where the two structures involved correspond to different arrangements of the nematic director. By studying wider cells, we show that the transition is in fact the usual isotropic-to-nematic (capillary) transition under confinement in the case of antagonistic surface forces. We show results for a wide range of values of film thickness and discuss the phenomenology using a mean-field model.

DOI: [10.1103/PhysRevE.83.041701](https://doi.org/10.1103/PhysRevE.83.041701)

PACS number(s): 61.30.Cz, 61.30.Hn, 61.20.Gy

## I. INTRODUCTION

The Lebwohl-Lasher lattice spin model [1] is an important model to understand the formation of the nematic phase in mesogenic materials. It provides qualitatively correct predictions and, in some cases, even quantitative information about nematic properties [2,3]. There is renewed interest in the model as regards the behavior of nematic films and the nature of the orientational phase transition. Also recently the confined model has been analyzed in hybrid geometry [4,5].

In the model, spin unit vectors  $\hat{s}$  are located at the sites of a cubic lattice of lattice parameter  $a$ . Nearest-neighbor (NN) spins interact via a potential energy  $-\epsilon P_2(\cos \gamma)$ , where  $\epsilon$  is a coupling parameter ( $\epsilon > 0$ ) and  $\cos \gamma = \hat{s} \cdot \hat{s}'$ , with  $\gamma$  the relative angle between the two spins.  $P_2(x)$  is the second-degree Legendre polynomial. In the confined model (see Fig. 1), parallel spin layers,  $h$  in number, are sandwiched between two planar, parallel plates (slit pore geometry), each formed by frozen spins that interact with spins in the first and last layers (those adjacent to the plates) also with the same potential, but with a (surface) coupling constant  $\epsilon_s$ . The Hamiltonian of the model is then

$$\mathcal{H} = -\epsilon \sum_{\text{NN}} P_2(\hat{s} \cdot \hat{s}') - \epsilon_s^{(1)} \sum_{\text{first layer}} P_2(\hat{m}_1 \cdot \hat{s}) - \epsilon_s^{(2)} \sum_{\text{last layer}} P_2(\hat{m}_2 \cdot \hat{s}), \quad (1)$$

where the first sum extends over all distinct NN spins, and the second and third only involve the spins in the first and last layers, respectively. The surface coupling constants  $\epsilon_s^{(i)}$ ,  $i = 1, 2$ , may or may not be different for both plates. In the

simulations to be presented below, we take  $\epsilon_s^{(1)}$  and  $\epsilon_s^{(2)}$  to be identical (in Sec. V the case of different constants will be considered) but, in general, each plate is assumed to favor a different spin orientation (easy axis),  $\hat{m}_1$  or  $\hat{m}_2$ . The case  $\hat{m}_1 = \hat{m}_2$  is a particular case, the symmetric cell, while  $\hat{m}_1 \neq \hat{m}_2$  is the asymmetric case, also called the hybrid or twisted cell, depending on the actual orientation of the axes. Since the number of fluctuating spin layers is  $h$ , the cell width is  $h + 1$  in units of the cubic lattice parameter  $a$ . The symmetry of the confined model implies that its properties only depend on the scalar  $\hat{m}_1 \cdot \hat{m}_2$ , and not on the individual components of the easy axes. In this respect, our cell is both hybrid (a name reserved for the case where one of the axes is normal to its surface, while the other is parallel) and twisted (a situation where the two axes lie on the surface planes).

The situation where  $\hat{m}_1 \cdot \hat{m}_2 = 0$  is very interesting, as the film will be subject to antagonistic but equivalent forces at the plates, which create frustration. The nematic director can satisfy both surface forces by rotating across the slab, creating an approximately linearly dependent, smoothly rotated director configuration (L phase), which involves an elastic energy. There have been two recent Monte Carlo (MC) simulations of this model [4,5], motivated by previous works that indicated the existence of a step-like slab configuration (S phase, sometimes called biaxial or exchange-eigenvector phase) in which the director is constant except in a thin central region, where it rotates abruptly between the two favored orientations [6–9]. These preliminary works, along with a more recent one on the twisted cell but with  $0 < \hat{m}_1 \cdot \hat{m}_2 \leq 1$  [10], are based on Ginzburg-Landau-type models and predict an L to S (LS) phase transition that was confirmed by the MC studies. A

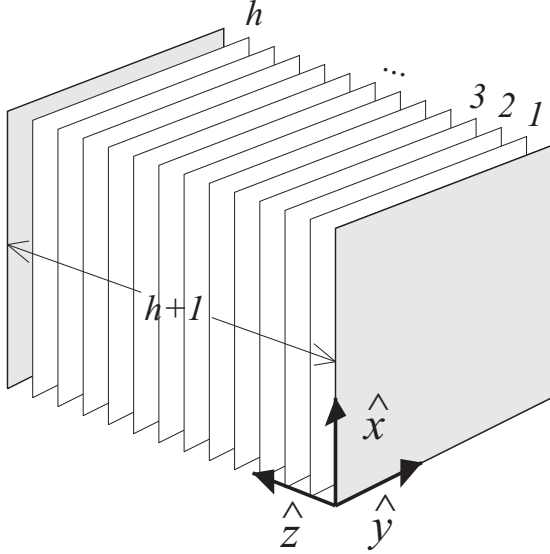


FIG. 1. Schematic representation of the confined Lebwohl-Lasher model.  $h$  is the number of spin layers sandwiched between the two external plates (shaded).  $h + 1$  is the film thickness in units of the cubic lattice parameter. The unit vectors along the Cartesian coordinates are indicated.

recent analysis of a hybrid cell using a surface-force apparatus may have detected this transition experimentally [11]. But the nature of the transition, the effect of plate separation, and especially the relationship between the LS transition and the bulk behavior (i.e., isotropic-nematic, or IN transition) have not been addressed in MC simulations. Some work on related, continuum nematic-fluid slabs under hybrid conditions, analyzed by means of density-functional theory, have appeared recently and partially answered some of these questions [12,13].

The MC results of Ref. [4] only presented a partial scenario of the problem. As mentioned, the connection of the LS transition with the bulk isotropic-nematic phase transition remained obscure, and the effect of plate strength  $\epsilon_s$  and the regime of very small separation were not explored. In a recent paper [5], the authors add some confusion to the problem by implicitly stating that there is a *second* transition in the slab, of unknown origin, inferred from a weak signal in the specific heat of the slab, as obtained from their MC simulations.

In the present paper we perform careful MC simulations on the hybrid cell with  $\epsilon_s^{(i)} = \epsilon$ ,  $i = 1, 2$ . These simulations will be supplemented by mean-field (MF) theoretical results, where cases with  $\epsilon_s^{(1)} \neq \epsilon_s^{(2)}$  will also be considered. We obtain the LS phase transition from specific-heat data obtained from long MC simulation runs, and extend the analysis to very small separations, including the case of a single spin layer. No additional transitions are observed in our simulations. The connection with the bulk IN transition is established by performing simulations on thicker nematic films, supplemented by MF calculations. The available evidence indicates that there is a single transition line in the phase diagram, namely the LS transition, and that this transition coincides with the capillary IN transition in the confined system, which is connected with the bulk IN transition as the plate separation  $h \rightarrow \infty$ .

In the remaining sections we first discuss the MC simulation techniques (Sec. II) and then show the results obtained for the

case of symmetric (Sec. III) and asymmetric (Sec. IV) plates. The MF model and its results are shown in Sec. V, which includes a discussion on the macroscopic approach (Kelvin equation) for this problem. The connection with the wetting properties is also discussed. A short discussion on the general picture and on the relation of the present results with those of Ref. [4] is given in Sec. VI. Conclusions are presented in Sec. VII. Some details of the macroscopic model can be found in the Appendices.

## II. MONTE CARLO TECHNIQUE

Let us take each of the  $h$  layers to consist of  $L \times L$  spins. The total number of spins is then  $N = hL^2$ . The MC simulation runs include two types of moves: one-particle orientational moves and cluster moves. The one-particle orientational moves are carried out using the standard algorithm for linear molecules described in Ref. [14]. The cluster moves are performed by means of the usual bonding criteria for NN particles [15,16]. The presence of the wall-particle interactions imposes some restrictions on the possible reflections that can be used to carry out the cluster moves. Notice, however, that the total energy is invariant with respect to a simultaneous change of sign of all the  $x$  components of the particle orientations. The same property applies to the  $y$  and  $z$  components. Therefore, in our realization of the cluster algorithm, we choose at random the component ( $s_x$ ,  $s_y$ , or  $s_z$ ) that will eventually flip. Then, we test the creation of bonds between every NN pair of particles by taking into account the change of interaction energy if only the coordinate of one of the particles of the pair is flipped, the bonding probability being [15–18]

$$b_{ij} = 1 - \exp \left\{ \min \left[ 0, \frac{-6\epsilon}{kT} (s_{\alpha i} s_{\alpha j} \hat{s}_i \cdot \hat{s}_j - s_{\alpha i}^2 s_{\alpha j}^2) \right] \right\}, \quad (2)$$

where  $\alpha = \{x, y, z\}$  is the chosen direction for the reflections,  $k$  is Boltzmann's constant, and  $T$  is the temperature. Once all the possible bonds have been tested, the actual bond realization is used to distribute the system in several clusters of particles. The cluster move is then performed following the Swendsen-Wang strategy [18]: Each cluster is flipped (or not flipped) with probability one-half.

The simulations were organized in blocks, each block containing 15 000 cycles. A cycle consists of  $N$  trial one-particle orientational moves and one cluster move. After an equilibration period of about 150 blocks, we calculate averages over 175 additional blocks of the potential energy per particle  $u$  and the eigenvectors and eigenvalues of different realizations of the local Saupe tensor  $\mathcal{Q}_i$  at each plane  $i = 1, \dots, h$ . This tensor has components

$$(\mathcal{Q}_i)_{\alpha\beta} = \frac{1}{L^2} \sum_{k \in \text{ith layer}} \frac{1}{2} (3s_{\alpha k} s_{\beta k} - \delta_{\alpha\beta}), \quad \alpha, \beta = x, y, z, \quad (3)$$

where the sum extends over all spins of the  $i$ th plane,  $L^2$  in number. The local tensor  $\mathcal{Q}_i$ , defined in each layer, is diagonalized, providing eigenvalues  $P_i$ ,  $-(P_i - B_i)/2$ , and  $-(P_i + B_i)/2$ . The first, associated with the  $x$  direction in the proper frame (i.e., the frame where  $\mathcal{Q}_i$  is diagonal), which coincides with the local nematic director  $\hat{n}_i$ , is the local uniaxial nematic order parameter, whereas  $B_i$  is the biaxial nematic order parameter. The orientation of the proper frame

with respect to the laboratory (plate-fixed) frame at each plane is given by the tilt angle  $\phi_i$ , which describes the director orientation in the  $xy$  plane (spanned by the plate orienting fields) and coincides with the angle between the  $x$  axes of the two frames. We define  $-\pi < \phi_i < \pi$ . For the symmetric cell, we take  $\hat{\mathbf{m}}_1 = \hat{\mathbf{m}}_2 = \hat{\mathbf{x}}$  and  $\langle \phi_i \rangle \simeq 0$ .  $\langle \dots \rangle$  denotes a thermal average over spin configurations. For the asymmetric cell, with  $\hat{\mathbf{m}}_1 \cdot \hat{\mathbf{m}}_2 = 0$  (we take  $\hat{\mathbf{m}}_1 = \hat{\mathbf{x}}$  and  $\hat{\mathbf{m}}_2 = \hat{\mathbf{y}}$ ), we compute, for each layer  $i$ , the angle  $\phi_i$  as

$$\cos \phi_i = \left( \frac{\langle n_{xi}^2 \rangle}{\langle n_{xi}^2 \rangle + \langle n_{yi}^2 \rangle} \right)^{1/2}, \quad (4)$$

where  $n_{xi}$  and  $n_{yi}$  are the  $x$  and  $y$  components of  $\hat{\mathbf{n}}_i$  (thermal averages of local quantities at sites lying in the same plane are identical by symmetry). Note that due to the high symmetry of the spin interaction, only one deformation mode of the angle  $\phi_i$  is possible in the cell (so that splay, bend, and twist are equivalent; see Appendix C). To analyze possible second-order phase transitions, we also compute an additional order parameter  $P_{xy}$  with

$$P_{xy} = \left\langle \frac{1}{N} \left| \sum_{k=1}^N s_{xk} s_{yk} \right| \right\rangle \quad (5)$$

and, for each plane  $i$ , the local order parameters

$$(P_{xy})_i = \left\langle \frac{1}{L^2} \left| \sum_{k \in i\text{th layer}} s_{xk} s_{yk} \right| \right\rangle. \quad (6)$$

The order parameter  $P_{xy}$  describes the global orientation of the particles in the plane of the interacting fields and is related to the thermal average of the absolute value of one of the off-diagonal elements of the Saupe tensor by  $P_{xy} = (2/3)\langle |Q_{xy}| \rangle$ . Likewise, global uniaxial and biaxial order parameters  $P$  and  $B$  can be defined:

$$P = \frac{1}{h} \sum_{i=1}^h P_i, \quad B = \frac{1}{h} \sum_{i=1}^h B_i. \quad (7)$$

Notice that these global order parameters do not correspond to those that could be computed by diagonalizing the global Saupe tensor. The following relation holds between  $P_i$ ,  $B_i$ ,  $(P_{xy})_i$ , and  $\phi_i$  locally (at each plane):

$$(P_{xy})_i = \frac{1}{2} \left( P_i - \frac{B_i}{3} \right) |\sin 2\phi_i|. \quad (8)$$

Therefore,  $(P_{xy})_i$  reflects the variations of both the nematic order parameters  $P_i$  and  $B_i$ , and of the director tilt angle  $\phi_i$ , across the slab. The LS transition can be monitored in principle by the changes with temperature of the global order parameters  $P$ ,  $B$ , and  $P_{xy}$ . As we will see, our simulations indicate that the transition in the confined slab has a continuous nature in the range of pore widths explored, so that these order parameters do not undergo discontinuities, but are singular in their derivatives. The associated singularities are washed out in our (necessarily) finite-size simulations. In fact, the finite-size dependence of the order parameters is very weak, and simulations on systems with large lateral sizes, along with a proper finite-size scaling analysis, are required. However, relevant response functions provide a more clear-cut signature of the transition.

We have focused on the excess heat capacity per spin,  $c_v = (\partial u / \partial T)_h$ , with  $u = \langle \mathcal{H} \rangle / N$  the average internal energy per spin. In the simulations  $c_v$  is obtained from the fluctuations in the energy. The phase-transition temperature will be located as that temperature at which  $c_v$  reaches a maximum value.

In order to locate the maximum in the heat capacity we use the synthetic method proposed by de Miguel [19], which we briefly describe in the following. Let us consider that  $c_{v_i}^{(0)}$  are the output values of the heat capacity and  $\Delta c_i$  their associated statistical errors as obtained from MC simulations at input temperatures  $T_i$ ,  $i = 1, \dots, n$ . Usually we fit  $c_{v_i}^{(0)}$  to a polynomial of order  $M$  in  $T$ ,  $c_v(T) = \sum_{i=1}^M a_i T^{i-1}$ . We search the maximum of this polynomial function by computing the value of the temperature  $T_m$  for which the derivative of the heat capacity with respect to the temperature is zero, then we calculate  $c_{v_m} = c_v(T_m)$ . The synthetic method consists of the following steps:

(i) Generate synthetic sets of  $n$  data points,  $c_{v_i}^{(k)} = c_{v_i}^{(0)} + \xi_i$ , where  $\xi$  is a random number drawn from a Gaussian distribution with zero mean value and standard deviation  $\Delta c_i$ .

(ii) Find the fitting coefficients  $a_i^{(k)}$  and calculate  $c_{v_m}^{(k)}$  corresponding to each synthetic set. The set of maximum heat capacities follows a Gaussian distribution, and we determine the mean value  $c_v^{\max}(L, h)$ .

Note that for each synthetic set generated we calculate  $T_m^{(k)}$ . This set of temperatures will also follow a Gaussian distribution, so we can determine the mean value, which will be denoted by  $T_c(L, h)$ .

### III. RESULTS FOR THE SYMMETRIC CELL

First we report on the case of symmetric plates,  $\hat{\mathbf{m}}_1 = \hat{\mathbf{m}}_2$ . This case has been investigated in detail by various authors, using MC simulation [20,21], MF theory [22,23], and renormalization-group (RG) techniques [24]. The cases  $\epsilon_s > 0$ , favoring positive order parameter, and  $\epsilon_s < 0$ , favoring negative order parameter, were considered. Here we focus on the first, using  $\epsilon_s^{(1)} = \epsilon_s^{(2)} = \epsilon$ . Mean-field models predict a

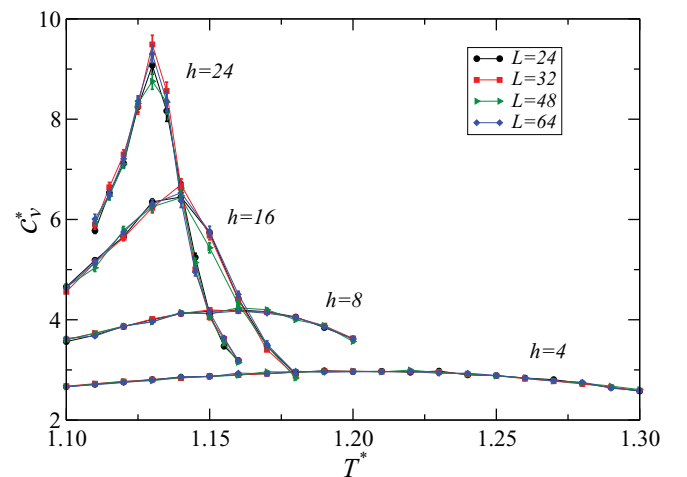


FIG. 2. (Color online) Excess heat capacity per spin in reduced units,  $c_v^*$ , as a function of reduced temperature  $T^*$ , for the symmetric case and for various plate separations (indicated as labeled). Several lateral sizes, given in the inset, are considered in each case.

weak first-order transition, and a terminal plate separation  $h_t$  below which the capillary isotropic-nematic transition disappears. The plain MF model gives  $h_t = 14$ , whereas a Bethe model, including two-spin correlations [23], increases the value up to  $h_t = 21$ . Assuming a monotonic variation due to higher order fluctuations, we may expect  $h_t \gtrsim 21$ . Simulations and RG calculations predict a continuous transition, in disagreement with MF results.

Our own simulation results were based on long runs using the special techniques described in the previous section. Our results, obtained for plate separations  $h \leq 24$ , are not compatible with the existence of a phase transition. Figure 2 shows the behavior of the heat capacity per spin,  $c_v^* = c_v/k$ , as a function of reduced temperature  $T^* = kT/\epsilon$ . Various plate

separations  $h$  are shown. In each case an analysis of how the lateral size of the sample  $L$  affects the results has been done. We can see that  $c_v$  does not show any significant dependence with  $L$  (provided that  $L > h$ ) as  $L \rightarrow \infty$ , even for  $h = 24$ . Therefore, we may expect  $h_t > 24$ .

#### IV. RESULTS FOR THE HYBRID CELL

The hybrid cell is the main focus of our work. For this cell we chose  $\mathbf{m}_1 = \hat{x}$  and  $\mathbf{m}_2 = \hat{y}$ . We have simulated systems with different number of slabs for plate strength  $\epsilon_s^{(1)} = \epsilon_s^{(2)} = \epsilon$ . In the following, detailed results are presented for the cases  $h = 8$ , which is representative of the LS phase transition within a narrow pore, and  $h = 1$ , which is a special case. At the end

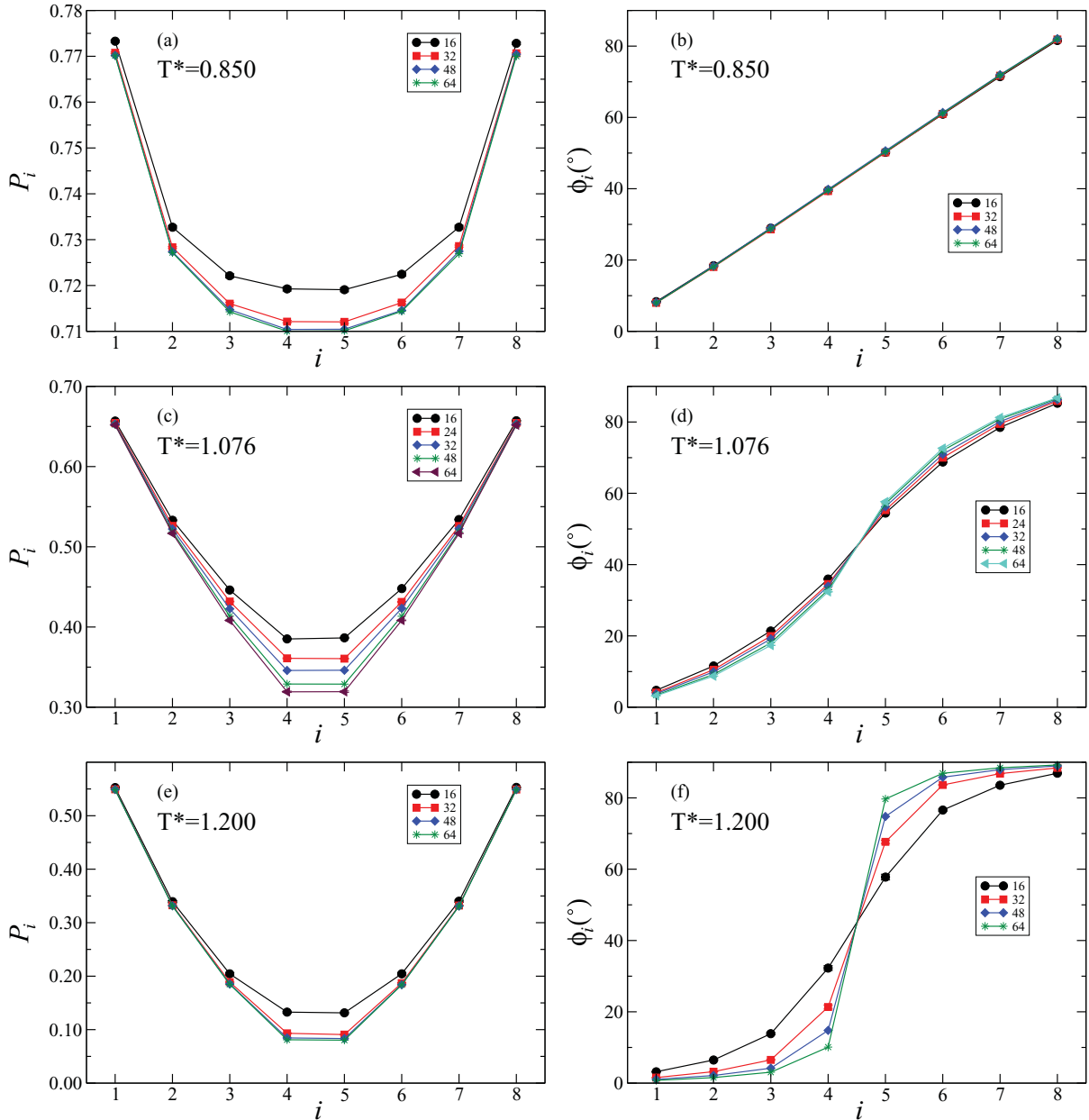


FIG. 3. (Color online) Nematic uniaxial order parameter  $P_i$  (left panels) and tilt angle of the nematic director  $\phi$  along the  $z$  direction for the slit pore with  $h = 8$ . (a) and (b)  $T^* = 0.850$ ; (c) and (d)  $T^* = 1.076$ ; (e) and (f)  $T^* = 1.200$ . The lateral size  $L$  used in the simulations is indicated in the insets.



of the section the global phase diagram, spanning a wide range of values of  $h$ , will be discussed. In particular, we show results for the case  $h = 32$ , which illustrate the nature of the LS phase transition in the regime of wide cells and are used to pinpoint the main differences with respect to the regime of narrow cells.

### A. $h = 8$

The uniaxial nematic order parameter  $P_i$  and the tilt angle  $\phi_i$  profiles are plotted in Fig. 3 for different values of reduced temperature. In agreement with earlier predictions found in the literature [4,5,12,13], the orientational structure changes *continuously* or *discontinuously* across the slab, depending on the temperature (obviously, one cannot strictly talk about continuous or discontinuous functions in a discrete system; these are fuzzy adjectives that we ascribe to an interpolating function, passing through all points in the profiles, that could reasonably be drawn in each case). For example, the tilt angle clearly shows that, for the highest temperature, there is a discontinuity in the center of the slab, this change becoming steeper as the system size is increased. This is the step-like (S) phase. By contrast, at low temperature, the orientation of the director changes smoothly from  $\hat{x}$  to  $\hat{y}$ : This is the linear-like (L) phase. At higher or lower temperatures no additional structural changes are visible in the order parameters or tilt angle. We conclude that there must be a temperature  $T_c$  at which the structure changes from the S to the L configuration as a thermodynamic phase transition and that, in view of the smooth variation of the profiles with temperature, one can assume this transition to be continuous. Later we will provide evidence that in the thermodynamic limit  $L \rightarrow \infty$ , the tilt-angle profile at the transition, corresponding to the situation depicted in Fig. 3(d), is actually a step function.

More information about the structural LS transition can be found by looking at the heat capacity. The phase transition is signaled by a diverging maximum of the heat capacity as the system lateral size is increased, Fig. 4(a). The maximum exhibits a linear dependence with  $\log L$ , as shown in Fig. 4(b). This dependence suggests that the confined Lebwohl-Lasher system under hybrid conditions for the case  $h = 8$  presents a continuous transition belonging to the universality class of the two-dimensional Ising model [25].

Such a hypothesis is fully supported by considering a cumulant analysis of spin correlations in the  $xy$  plane. Specifically, we define a global Saupe tensor as

$$Q = \frac{1}{h} \sum_{i=1}^h Q_i \quad (9)$$

and focus on the tensor element  $Q_{xy}$ . The finite-size dependence [25] of the quantity  $G_4 \equiv \langle Q_{xy}^4 \rangle / \langle Q_{xy}^2 \rangle^2$  turns out to be fully consistent with the proposed critical behavior. The results for  $h = 8$  and different values of  $L$  are presented in Fig. 5. As expected, the different curves intersect at values of  $G_4$  not too far from the universal value  $G_{4c} \simeq 1.168$  of the two-dimensional Ising universality class for systems with  $L_x = L_y$  and periodic boundary conditions [26]. Then we assume the scaling relation [25]

$$T_c(L, h) = T_c(h) + aL^{-1/\nu}, \quad (10)$$

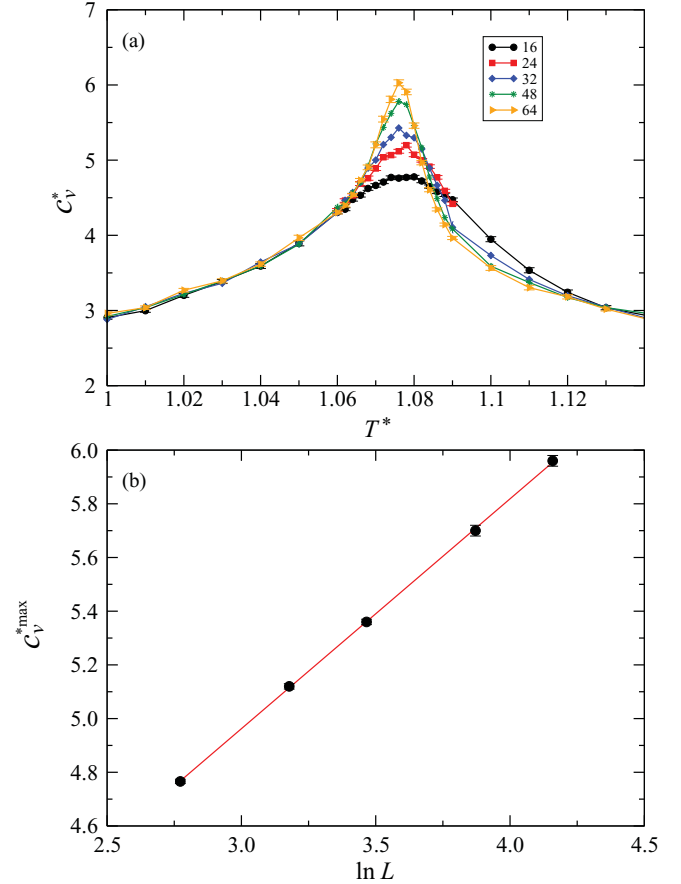


FIG. 4. (Color online) (a) Excess heat capacity per spin in reduced units,  $c_v^*$ , for the system with  $h = 8$ , as a function of reduced temperature  $T^*$  and for different lateral system sizes  $L$  (indicated in the inset). (b) Maximum of the heat capacity per spin in reduced units,  $c_v^{*max}$ , for the system with  $h = 8$ , as a function of lateral system sizes  $L$ . The straight line is a linear fit.

where the critical exponent has the value  $\nu = 1$  for the two-dimensional Ising universality class [26], and obtain the critical

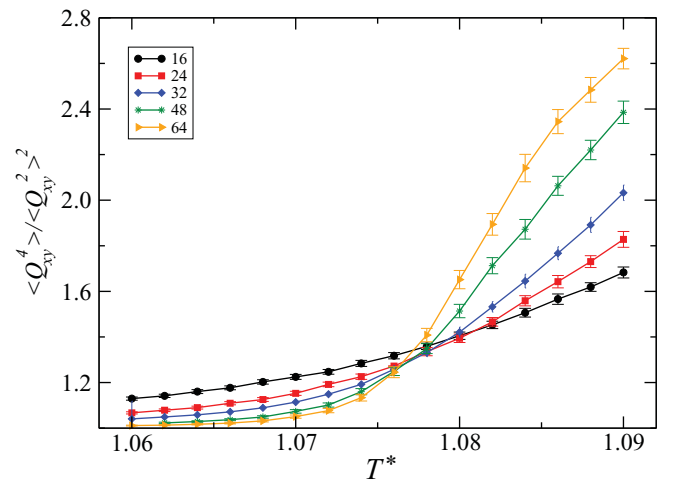


FIG. 5. (Color online) Dependence of the normalized fourth-order cumulant  $G_4 = \langle Q_{xy}^4 \rangle / \langle Q_{xy}^2 \rangle^2$  with reduced temperature  $T^* = kT/\epsilon$  and lateral size  $L$  for the system with  $h = 8$ . The lateral size of the systems is quoted in the legend.

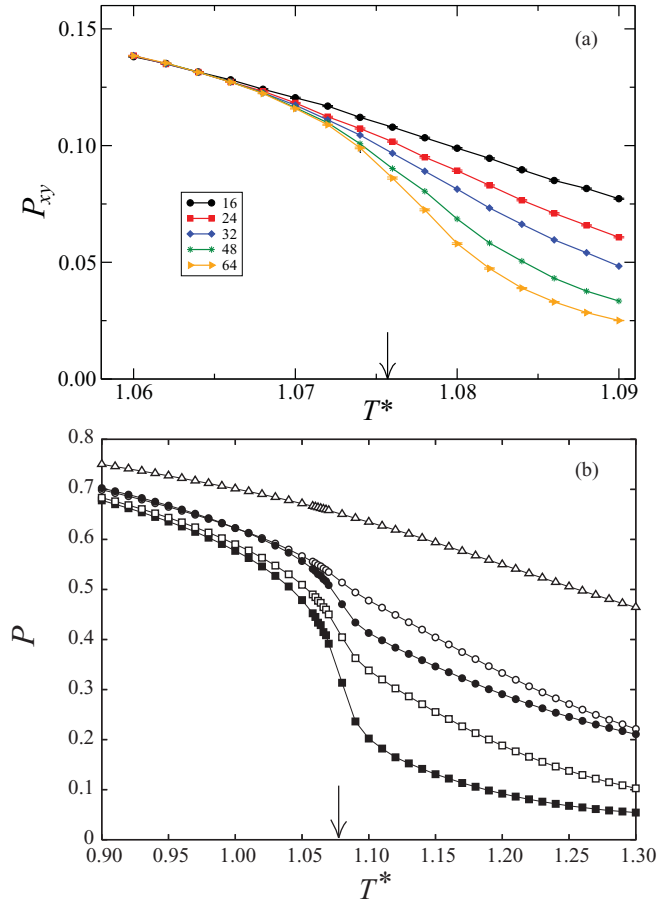


FIG. 6. (Color online) Order parameters (a)  $P_{xy}$  and (b)  $P$  as a function of temperature  $T$ , both for pore width  $h = 8$ . (a) Different curves give  $P_{xy}$  for different values of lateral size  $L$  (see key). (b) Order parameter  $P_i$  for  $i = 1$  (triangles),  $i = 2$  (open circles),  $i = 3$  (open squares), and  $i = 4$  (filled squares) for lateral size  $L = 32$ . The global order parameter  $P$  is represented by filled circles. In both (a) and (b) the vertical arrow indicates the location of the phase transition as estimated from the heat capacity.

temperature of the transition as  $T_c(h) = \lim_{L \rightarrow \infty} T_c(L, h)$ . For the particular value of cell thickness  $h = 8$  we obtain  $T_c^*(h = 8) = 1.076(1)$ .

In Fig. 6 we present results for the quantities  $P_{xy}$ ,  $P$ , and  $P_i$  as a function of temperature for the fixed pore width  $h = 8$ . In Fig. 6(a) the dependence of  $P_{xy}$  on lateral size  $L$  is shown. We see that lateral size hardly affects the value of  $P_{xy}$  in the L phase (low temperatures), while the value in the S phase (high temperatures) decreases with lateral size (the location of the transition is indicated by an arrow). There is no clear signature of the transition at the level of  $P_{xy}$ . To check whether  $P_{xy} \rightarrow 0$  in the S phase in the thermodynamic limit, we have performed extensive simulations for systems with rather large lateral size. The results are plotted in Fig. 7, which represents  $L^{1/8} P_{xy}$  as a function of  $L^{-1}$  (the exponent  $1/8$  corresponds to a two-dimensional Ising-like critical transition). From these results one can conclude that the transition has a two-dimensional character, at least for the pore size  $h = 8$  and smaller (the nature of the transition should change to first order for sufficiently wide pores, see discussion in Sec. IV C).

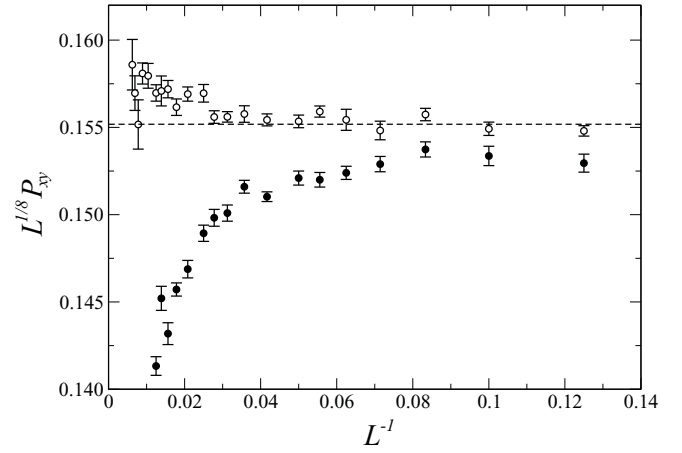


FIG. 7. Dependence of the order parameter  $P_{xy}$  on the lateral size  $L$  of the system for two different values of scaled temperature which are close to the true critical temperature, for the case  $h = 8$ . Filled circles:  $T^* = 1.076$ . Open circles:  $T^* = 1.075$ . Error bars are included in each case. The horizontal line indicates an approximate value of  $L^{1/8} P_{xy}$  for the latter temperature in the thermodynamic limit  $L \rightarrow \infty$ .

The uniaxial order parameter  $P_i$  is plotted in Fig. 6(b) for a fixed lateral size of  $L = 32$  and for the different planes  $i = 1, 2, 3$ , and 4 (planes with  $i = 8, 7, 6$ , and 5 are symmetric). The global order parameter  $P$  is also plotted. At the transition (indicated by an arrow) the order parameter shows a larger variation, but again no anomaly can be seen. Note that the variation with temperature is more abrupt for the planes closer to the middle of the pore, which is the region where the director is having more dramatic rearrangements. As opposed to  $P_{xy}$ , the global uniaxial order parameter  $P$  should be finite in the thermodynamic limit at the transition, and in this limit a kink should exist; again the finite lateral size prevents this anomaly from showing up.

The picture that emerges from these results is that, starting from the low-temperature region, where the L phase is stable, and upon approaching the transition by increasing the temperature, the director tilt angle starts to bend from the linear-like configuration and ultimately develops an abrupt variation that becomes a step at the transition [so that  $(P_{xy})_i = 0$  at each plane, implying  $\sin 2\phi_i = 0$ ]. This conclusion is subtle, as it implies that the tilt-angle profiles shown in Fig. 3(d) for the critical configuration actually tend toward a step function in the thermodynamic limit  $L \rightarrow \infty$ .

The physical nature of the phase transition is easily explained as a competition between the anchoring effect of the walls, which the film tries to satisfy simultaneously but creates conflicting director orientations at the two walls, and the elastic energy incurred when the director rotates between one orientation and the other. At low temperatures or large film thickness, the system can accommodate a linearly rotating director in the film. When the temperature is high or the film thin, the system prefers to eliminate the (large) elastic contribution at the cost of creating a step configuration, which can be regarded as a planar defect.

The L phase is degenerate in the following sense. As one goes from  $z = 1$  to  $z = h$  through a line of sites with equal

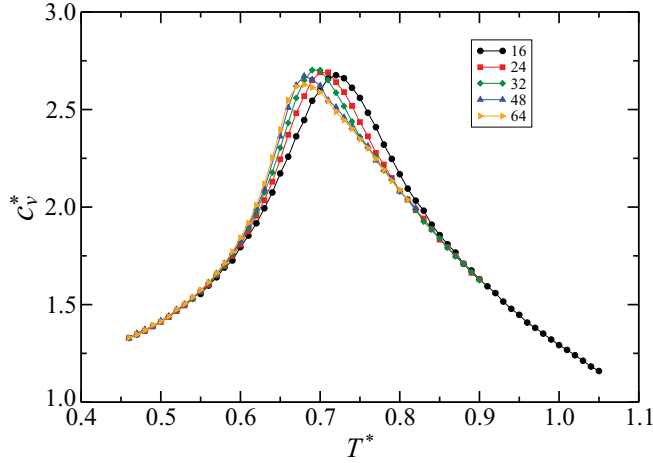


FIG. 8. (Color online) Variation of the excess heat capacity per particle  $c_v^*$  with reduced temperature  $T^*$  for  $h = 1$  and different values of  $L$  (indicated in the inset).

values of  $x$  and  $y$ , the orientation of the spins rotates from  $\hat{x}$  to  $\hat{y}$ . This rotation can be clockwise (+) or anticlockwise (-). The NN interactions between sites impose correlations between pairs of NN site lines, which make favorable that two NN lines have the same rotation sign. Below  $T_c$  the system chooses (with equal probability) either + or - as the preferred orientation sign.

### B. $h = 1$

The case  $h = 1$  (single layer) is special. Here the spins are subject to an azimuthally invariant potential that favors spin configurations parallel to the plates. Therefore the transition belongs to the XY universality class. In fact, our results for the heat capacity (see Fig. 8 and Table I) and the behavior of the nematic order parameter (see Fig. 9) suggest that the transition is of the Berezinskii-Kosterlitz-Thouless (BKT) [27,28] type. The heat capacity shows a maximum, but  $c_v^{\max}(L)$  hardly depends on system size and presents a shift toward slightly lower temperatures as  $L$  increases. For a given system

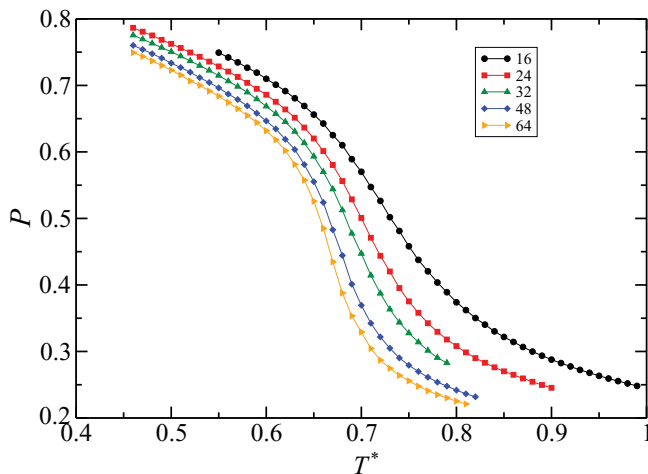


FIG. 9. (Color online) Behavior of the nematic order parameter  $P$  as a function of reduced temperature  $T^*$  for  $h = 1$  and various lateral sizes  $L$  (indicated in the inset).

TABLE I. Maximum excess heat capacity per particle and the corresponding temperatures  $T_{\max}$  and pseudocritical temperatures  $T_c(L)$ , defined as indicated in the text, for the hybrid nematic film for pore width  $h = 1$ .

	$L = 16$	$L = 24$	$L = 32$	$L = 48$	$L = 64$
$c_v^{\max}(L)/k$	2.661(3)	2.668(3)	2.696(4)	2.628(3)	2.614(3)
$T_{\max}^*(L)$	0.7210(7)	0.7040(5)	0.6940(7)	0.6872(4)	0.6858(4)
$T_c^*(L)$	0.723(1)	0.703(1)	0.691(1)	0.678(1)	0.669(1)

size  $L$  we consider the temperature at which  $|dP/dT|$  is maximum as the corresponding pseudocritical temperature  $T_c(L)$ . With the values for different system sizes a rough estimation of the transition temperature in the thermodynamic limit,  $T_{\text{BKT}} = \lim_{L \rightarrow \infty} T_c(L)$ , can be obtained by fitting the results to the equation [29]

$$T_c(L) \simeq T_{\text{BKT}} + a(\log L)^{-2}. \quad (11)$$

With this scheme we obtain  $T_{\text{BKT}}^* = T_c^*(h = 1) \simeq 0.63 \pm 0.01$ .

### C. Wide pores and global phase diagram

Using the techniques explained in the previous sections, we have extended the calculation of the LS transition to other values of pore width  $h$ . The values of  $T_c(L, h)$  obtained from the heat capacity are used to extrapolate to the thermodynamic limit, using Eq. (10). The results of this fitting for the different values of  $h$  explored are gathered in Table II. As can be seen, the critical temperature  $T_c(h)$  increases monotonically with  $h$  and approaches the value of the bulk isotropic-nematic transition temperature,  $T_{\text{IN}}^* = 1.1225(1)$  [16,30]. One important point is that only a single peak is observed in the specific heat in all cases as  $T$  is varied, indicating the presence of a single transition in this system. Therefore, our data do not corroborate the findings of Chiccoli *et al.* [5], who claim the existence of two distinct peaks in the heat capacity.

The resulting phase diagram in the plane  $T-h^{-1}$  is presented in Fig. 10. The interval  $0 \leq h^{-1} \leq 1$  was covered in the MC simulations (the bulk,  $h^{-1} = 0$ , value was obtained from independent simulations in Ref. [16,30]). The maximum plate separation considered for the confined fluid was  $h = 32$ , which increases the maximum value used in [4] and [5]. The LS transition line spans the whole interval  $0 \leq h^{-1} \leq 1$ . For the plate separations explored,  $1 \leq h \leq 32$ , the transition is continuous. As mentioned before, since the bulk transition is of (weakly) first order, there must be a change from first order to continuous behavior at some (probably large) value of  $h$ .

TABLE II. Estimates of the transition temperatures for the hybrid nematic films. Error bars are given between parentheses, in units of the last figure quoted, and correspond to 95% confidence level.

$h$	2	4	8	16	32
$T_c^*(h)$	0.817(1)	0.994(2)	1.076(1)	1.108(1)	1.119(1)

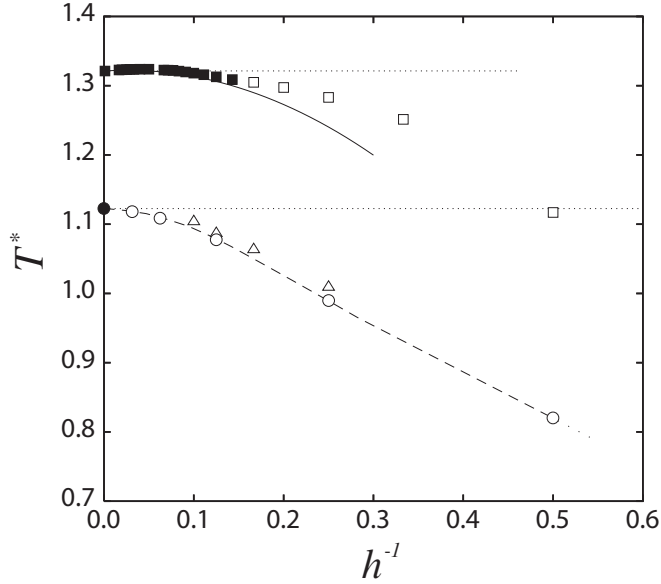


FIG. 10. Phase diagram for the hybrid cell in the  $T^*$ - $h^{-1}$  plane for the case  $\epsilon_s^{(1)} = \epsilon_s^{(2)} = \epsilon$ , showing temperatures at which the LS transition occurs for each value of plate separation. L (S) phase is stable below (above) the corresponding symbol. Circles: Present MC simulation results. Triangles: MC simulation results by Chiccoli *et al.* [4]. Squares: Present MF results. Filled symbols represent first-order phase transitions, while open ones refer to continuous phase transitions. Horizontal dotted lines: Bulk temperatures as obtained from the MF and MC calculations (upper and lower lines, respectively). Continuous line: Modified Kelvin equation. Dashed line is a guide to the eye.

As the transition line is crossed at fixed  $h$ , the spin structure in the slab changes suddenly but continuously, as it corresponds to the continuous phase transition discussed in Sec. IV A. Here we show profiles for the cases  $h = 8$  and  $h = 32$ , in order to illustrate the differences between narrow and wide pores. Figure 11 shows the change in structure for the cases  $h = 8$  and  $32$  as the temperature is increased, reflected by the values of the order parameters  $P_i$  and  $(P_{xy})_i$ , and by the director tilt angle  $\phi_i$ . At high temperature [Figs. 11(c) and 11(f)] the structure is of the S type, with an abrupt change in the tilt angle as the middle plane of the slab is crossed, and with a low value of the order parameter  $P$  in the central region. As  $T$  is lowered, we pass from the S to the L structure, with the tilt angle slowly rotating from one plate to the other. Note that the value of the order parameter  $P_i$  in the center of the slab increases substantially at the transition [which occurs in the situations represented by panels (b) and (e)]. In the S phase the difference between the two cases shown in the figure, which may be representative of a thin ( $h = 8$ ) and a thick ( $h = 32$ ) slab, is that, in the thick-slab case, the nematic films next to the plates are more separated, leaving a wider orientationally disordered region in the central part of the slab. The reason why the central region of the pore is not completely disordered, panel (f), may be a finite-size effect. Indeed, as discussed in Sec. IV A (see Fig. 7), we expect a step function behavior for  $\phi_i$  at the transition [panel (e)] in the thermodynamic limit, while  $P_i$  should go to zero right at the middle of the pore, and  $(P_{xy})_i$  should be zero everywhere.

Therefore, in the situation described in panel (f), the tilt-angle profile should be a step function, while the  $P_i$  profile would be expected to exhibit a wide gap with  $P_i \simeq 0$ , i.e. a thick isotropic central slab. As  $h$  is increased, this central region will become thicker, implying that the S phase is the confined phase connected with the *bulk* isotropic phase. On the low- $T$  side, the linear-like phase is the confined nematic phase and it evolves to the *bulk* nematic phase (with a director that rotates more and more slowly across the slab). The LS transition is the isotropic-to-nematic (IN) transition in a hybrid cell, and no additional capillary or structural transitions should be expected to occur in this system.

As a final comment, we note that the MC data for the transition points obtained by Chiccoli *et al.* [4] are slightly shifted with respect to our own data. These differences may result from the more efficient sampling of the present study, which considers cluster algorithms in the MC moves. Also, our simulations are longer, maximum lateral sizes are larger, and a proper finite-size calculation of the transition temperature is performed.

## V. MEAN-FIELD MODEL

The MF theory for the Lebwohl-Lasher model has been used before to study symmetric nematic slabs [21–23]. A rich phase diagram with respect to the parameters  $T$  and  $h$  and the surface couplings results. Here we use the model to rationalize the MC findings shown in the previous section, focusing on the hybrid cell. First we briefly comment on the implementation of the theory and then present the results and their connection with the macroscopic behavior.

### A. Theory and method of solution

The orientational distribution of a spin in the  $i$ th plane is given by the function  $f_i(\hat{s})$ . The complete MF free-energy functional for the Lebwohl-Lasher model is

$$\begin{aligned}
 \frac{F[\{f_i\}]}{L^2} = & kT \sum_{i=1}^h \int d\hat{s} f_i(\hat{s}) \log [4\pi f_i(\hat{s})] \\
 & - 2\epsilon \sum_{i=1}^h \int d\hat{s} \int d\hat{s}' f_i(\hat{s}) f_i(\hat{s}') P_2(\hat{s} \cdot \hat{s}') \\
 & - \epsilon \sum_{i=1}^{h-1} \int d\hat{s} \int d\hat{s}' f_i(\hat{s}) f_{i+1}(\hat{s}') P_2(\hat{s} \cdot \hat{s}') \\
 & - \epsilon_s^{(1)} \int d\hat{s} f_1(\hat{s}) P_2(\hat{s} \cdot \hat{m}_1) \\
 & - \epsilon_s^{(2)} \int d\hat{s} f_h(\hat{s}) P_2(\hat{s} \cdot \hat{m}_2) - \sum_{i=1}^h \lambda_i \int d\hat{s} f_i(\hat{s}).
 \end{aligned} \tag{12}$$

The  $\lambda_i$ 's are Lagrange multipliers ensuring the normalization  $\int d\hat{s} f_i(\hat{s}) = 1$ . The interaction part contains contributions from spins on the same layer and from spins on two neighboring layers, and also from the external potentials. Here we find it more convenient to use  $\hat{m}_1 = \hat{x}$  and  $\hat{m}_2 = \hat{z}$  as easy axes.



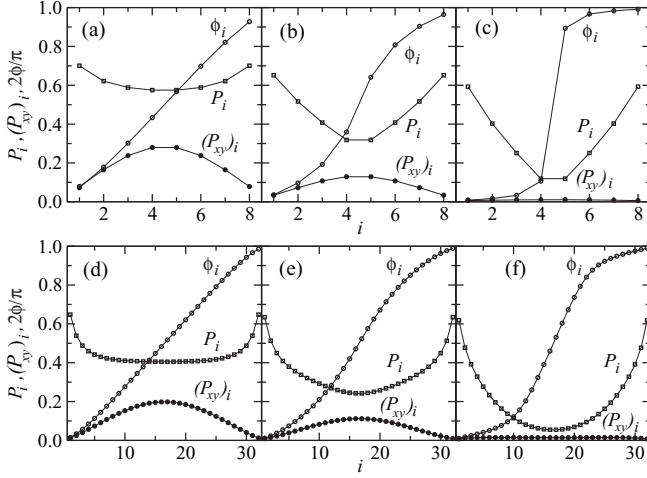


FIG. 11. Local order parameters  $P_i$ ,  $(P_{xy})_i$  and director tilt angle  $\phi_i$  obtained from the MC simulations for two different pore widths,  $h = 8$  ( $L = 64$ ) and  $h = 32$  ( $L = 48$ ), at various temperatures in the neighborhood of the corresponding critical temperature  $T_c(h)$ . (a)  $h = 8$  and  $T^* = 1$ ; (b)  $h = 8$  and  $T^* = 1.076$ ; (c)  $h = 8$  and  $T^* = 1.15$ ; (d)  $h = 32$  and  $T^* = 1.101$ ; (e)  $h = 32$  and  $T^* = 1.118$ ; (f)  $h = 32$  and  $T^* = 1.135$ . Notice that for  $T > T_c$  the jump in  $\phi$  is system-size ( $L$ ) dependent, and becomes steeper as  $L$  approaches the thermodynamic limit.

Functional minimization of  $F$  provides the corresponding coupled, self-consistent Euler-Lagrange equations for each plane, which are projected onto a spherical-harmonics basis using

$$f_i(\hat{s}) = \sum_{l=0}^{\infty} \sum_{m=-l}^l f_{lm}^{(i)} Y_{lm}(\hat{s}). \quad (13)$$

As usual in MF theory, the corresponding equations can be interpreted as if each spin felt an effective field created by their neighbors. The effective field is given by the functions  $\Phi^{(\alpha)}(\hat{s})$ , with

$$\begin{aligned} \Phi^{(0)}(\hat{s}) &= P_2(\cos \theta), & \Phi^{(1)}(\hat{s}) &= \sin 2\theta \cos \varphi, \\ \Phi^{(2)}(\hat{s}) &= \sin^2 \theta \cos 2\varphi, \end{aligned} \quad (14)$$

and  $(\theta, \varphi)$  the spherical angles of the spin  $\hat{s}$ . Instead of using the whole distribution functions  $f_i(\hat{s})$ , the order will be described by three laboratory-fixed order parameters,  $\eta_i^{(\alpha)}$  where  $\alpha = 0, 1, 2$ , and  $i = 1, \dots, h$  runs through the  $h$  layers. The order parameters are related to the  $l = 2$  subspace coefficients  $f_{lm}^{(i)}$  by  $f_{20}^{(i)} = \eta_i^{(0)} \sqrt{5/4\pi}$ ,  $f_{21}^{(i)} = -f_{2,-1}^{(i)} = -\eta_i^{(1)} \sqrt{5/6\pi}$  and  $f_{22}^{(i)} = f_{2,-2}^{(i)} = \eta_i^{(2)} \sqrt{5/6\pi}$ . In terms of  $\eta_i^{(\alpha)}$ , the Euler-Lagrange equations are written

$$\eta_i^{(\alpha)} = \langle \Phi^{(\alpha)}(\hat{s}) \rangle_i, \quad i = 1, 2, \dots, h, \quad (15)$$

where  $\langle \dots \rangle_i$  are averages over the orientational distribution function  $f_i(\hat{s})$ , with

$$f_i(\hat{s}) \propto \exp \left[ \beta \epsilon \sum_{\alpha=0}^2 (4\eta_i^{(\alpha)} + \eta_{i-1}^{(\alpha)} + \eta_{i+1}^{(\alpha)}) \Phi^{(\alpha)}(\hat{s}) + \Phi_i^{(s)}(\hat{s}) \right], \quad (16)$$

where  $\beta = 1/kT$ . In this expression  $f_i(\hat{s})$  has to be normalized to unity, and we take  $\eta_0^{(0)} = -1/2$ ,  $\eta_0^{(1)} = 0$ ,  $\eta_0^{(2)} = 1$ ,  $\eta_{h+1}^{(0)} = 1$ ,  $\eta_{h+1}^{(1)} = 0$ , and  $\eta_{h+1}^{(2)} = 0$ .  $\Phi_i^{(s)}(\hat{s})$  are surface fields, with the properties

$$\Phi_i^{(s)}(\hat{s}) = \begin{cases} -\frac{\epsilon_s^{(1)}}{2} [\Phi^{(0)}(\hat{s}) - \frac{3}{2}\Phi^{(2)}(\hat{s})], & i = 1, \\ 0, & 1 < i < h, \\ \epsilon_s^{(2)}\Phi^{(0)}(\hat{s}), & i = h. \end{cases} \quad (17)$$

The order parameters  $\eta_i^{(\alpha)}$  are related to the eigenvalues of the order tensor,  $P_i$  (uniaxial) and  $B_i$  (biaxial) order parameters, and the director tilt angle  $\phi_i$ , through the relations

$$\eta_i^{(0)} = P_i P_2(\cos \phi_i) + \frac{3}{4} B_i \sin^2 \phi_i,$$

$$\eta_i^{(1)} = \left( \eta_i^{(0)} - \frac{\eta_i^{(2)}}{2} \right) \tan 2\phi_i,$$

$$\eta_i^{(2)} = P_i \sin^2 \phi_i + \frac{1}{2} B_i (1 + \cos^2 \phi_i).$$

Here  $\phi_i$ , for the sake of convenience, is measured with respect to the  $z$  axis (we remind the reader that, due to the symmetry of the model, this angle is the same as the one used in the MC simulations). From these equations, we can obtain  $P_i$ ,  $B_i$ , and  $\phi_i$  from  $\eta_i^{(0)}$ ,  $\eta_i^{(1)}$ , and  $\eta_i^{(2)}$ . For the bulk system the surface fields are eliminated and  $\eta_i^{(0)} = P$ ,  $\eta_i^{(1)} = \eta_i^{(2)} = 0$ . The isotropic-nematic phase transition is of first order and occurs at  $T^* = 1.321$ . The order parameter at the transition is  $P = 0.429$ .

## B. Results: identical surface couplings

In this section we consider the confined case and take  $\epsilon_s^{(1)} = \epsilon_s^{(2)} = \epsilon$ . These values ensure that, at bulk conditions, both surfaces are wet by the nematic phase (see Appendix A) so that, close to the bulk transition temperature  $T_{IN}$ , thick nematic films are expected at both surfaces.

Order-parameter and tilt-angle profiles are shown in Fig. 12 for the cases  $h = 8$  and  $9$  at the corresponding transition temperatures. The L and S structures coexist at a first-order phase transition, in contrast to the MC results, which indicate a continuous transition. As in the case of the MC results deep into the S phase, we note the clear discontinuity in the director tilt angle in the coexisting S phase. In the coexisting L phase the director configuration adopts a linear-like configuration. We also note that at the transition, the nematic order parameter  $P$  changes quite substantially: In the S phase two nematic slabs meet at the central region, such that the central spins are almost completely disordered, whereas the L phase corresponds to a well-developed nematic slab. The differences between the cases where  $h$  is an even or odd number are apparent by comparing the cases  $h = 8$  and  $h = 9$ . While the L phase hardly changes, the S phase of the even- $h$  case does not have a negligible value of the order parameter  $P$  at the central region, in contrast with the midpoint of the odd- $h$  slab. The biaxial order parameter  $B$  is nonnegligible only in the neighborhood of the step. The uniaxial order parameter and director tilt angle profiles obtained from the MF theory are quite similar

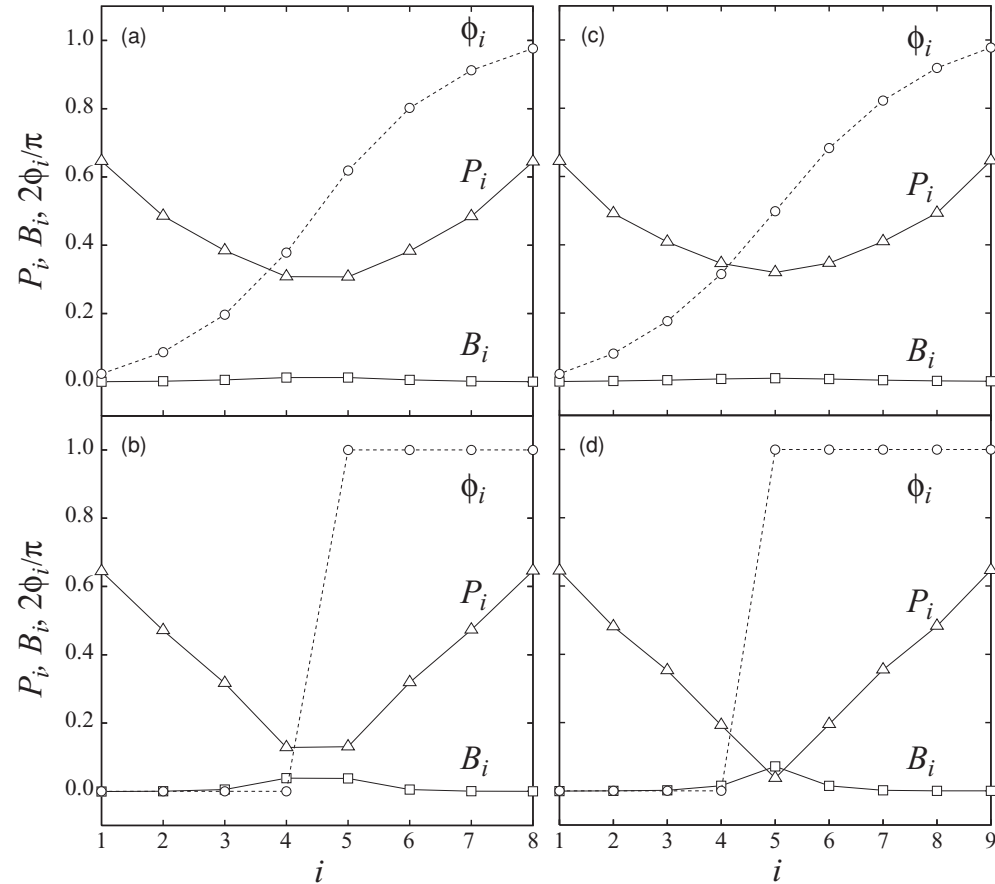


FIG. 12. Order parameters  $P_i$  and  $B_i$  and director tilt angle  $\phi_i$  for the two phases coexisting at the LS phase transition, in the case  $\epsilon_s^{(1)} = \epsilon_s^{(2)} = \epsilon$  and as obtained from MF calculations. (a) L phase for  $h = 8$ ; (b) S phase for  $h = 8$ ; (c) L phase for  $h = 9$ ; (d) S phase for  $h = 9$ .

to those from MC simulation [cf. the two coexisting phases of Figs. 12(a) and 12(b) with the structures shown in Figs. 11(a) and 11(c)].

The nature of the LS transition becomes evident if we look at a wider pore. This is shown in Fig. 13, which corresponds to  $h = 32$ . In this case the high-temperature S phase has a large central region with a virtually zero value of  $P$ . As the transition is crossed from the region of high temperature, the value of  $P$  in the central region increases to a nematic-like value, and the total order parameter in the cell undergoes a discontinuous change. Therefore this transition, which corresponds to the capillary isotropic-nematic transition, is the same as the LS transition, and it can be concluded that there is a single transition line in the phase diagram. Note that the phase corresponding to Fig. 13(b) (confined isotropic phase, with two differently-oriented nematic slabs adsorbed at each plate) for  $h = 32$  is smoothly connected to that of Figs. 12(b) for  $h = 8$  or 12(d) for  $h = 9$  (the step-like phase), since they are actually the same phase but with an “isotropic” central slab of different width.

The MF phase diagram, in the plane  $T$  vs.  $h^{-1}$ , is presented in Fig. 10. Transition temperatures for the different values of  $h$  explored are represented by squares. Note that the character of the transition changes from first order (for  $h \geq 7$ ) to continuous (for  $h \leq 6$ ). The main differences between the MF results

and the MC simulations are as follows: (i) The transition is weakly of first order in MF for  $h \geq 7$ ; in the simulations it is continuous for the range of plate separations explored (as mentioned already, the transition must change to first order at some, probably large, value of  $h$ , since it is of first order in bulk). (ii) There is a shift in the transition to higher values of  $T$  in MF, in correspondence with the shift in the bulk transition. (iii) In the simulation, the transition line seems to tend to the bulk value from below, with a very small slope at the origin  $h^{-1} = 0$  (see Fig. 10); in the MF theory, it changes slope and actually crosses the bulk temperature at  $h \simeq 12$  (see Fig. 15, where an enlarged phase diagram is presented).

In Fig. 14 we plot the order parameters  $P$  and  $P_{xy}$  as a function of reduced temperature  $T^*$  for the case  $h = 60$  [panel (a)], where the LS transition is of first order, and  $h = 5$  [panel (b)], where the transition is continuous. The behavior of the order parameters reflected in the figures may be qualitatively similar to the real situation. In (a), both order parameters undergo discontinuous changes, indicated by the dotted vertical lines (the sharp variation in  $P$  in the metastable step-like branch below the transition corresponds to the frustrated wetting transition at each plate due to the confinement). In panel (b) both order parameters are continuous but exhibit a “kink” at the LS transition. Note that  $P_{xy}$  is always zero in the step-like

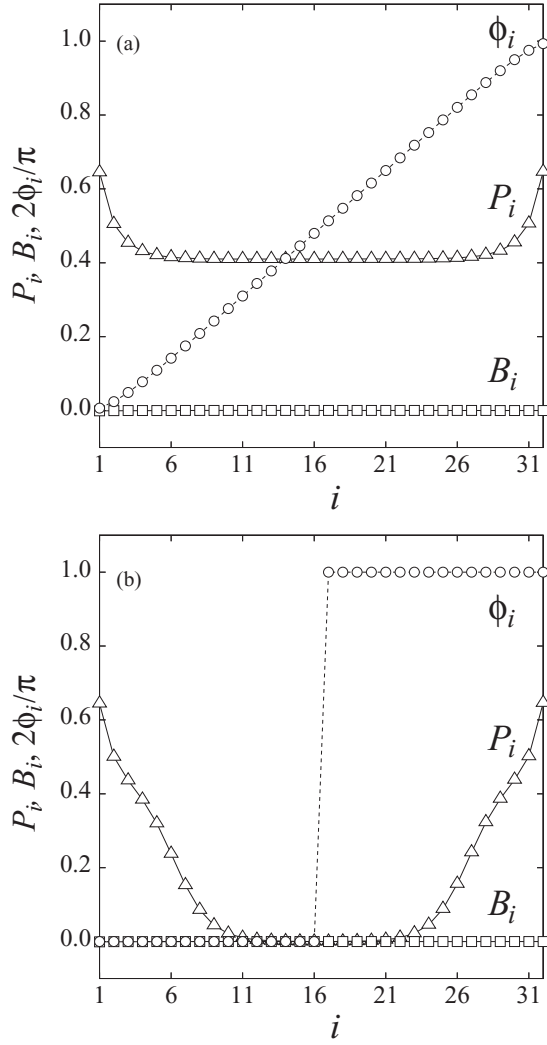


FIG. 13. Order parameters  $P_i$  and  $B_i$  and director tilt angle  $\phi_i$  for the two phases coexisting for a pore width  $h = 32$ , as obtained from the MF calculations in the case  $\epsilon_s^{(1)} = \epsilon_s^{(2)} = \epsilon$ . (a) L phase. (b) S phase.

phase, implying that the director tilt-angle is a perfect step function.

### C. Results: other surface couplings

We now discuss the case where the surface coupling constants are different. This situation is closer to the experiments. We analyze cases where the couplings of the two surfaces are different, and also consider situations where conditions of complete wetting by nematic prevail, as well as cases where one or the two surfaces are not wet by the nematic phase.

(1) In the first case, the surface couplings are chosen as  $(\epsilon_s^{(1)}, \epsilon_s^{(2)}) = (\epsilon, 0.4\epsilon)$ , which again ensures a regime of complete wetting by the nematic phase at the two surfaces (see Appendix A). Therefore thick nematic films are expected at both surfaces for temperatures close to the bulk transition temperature. In this case the LS phase-transition curve shifts to lower temperatures with respect to the previous case, but by a small amount, as evident from Fig. 15. From a structural point of view, the change involves a shift in the location of the step:

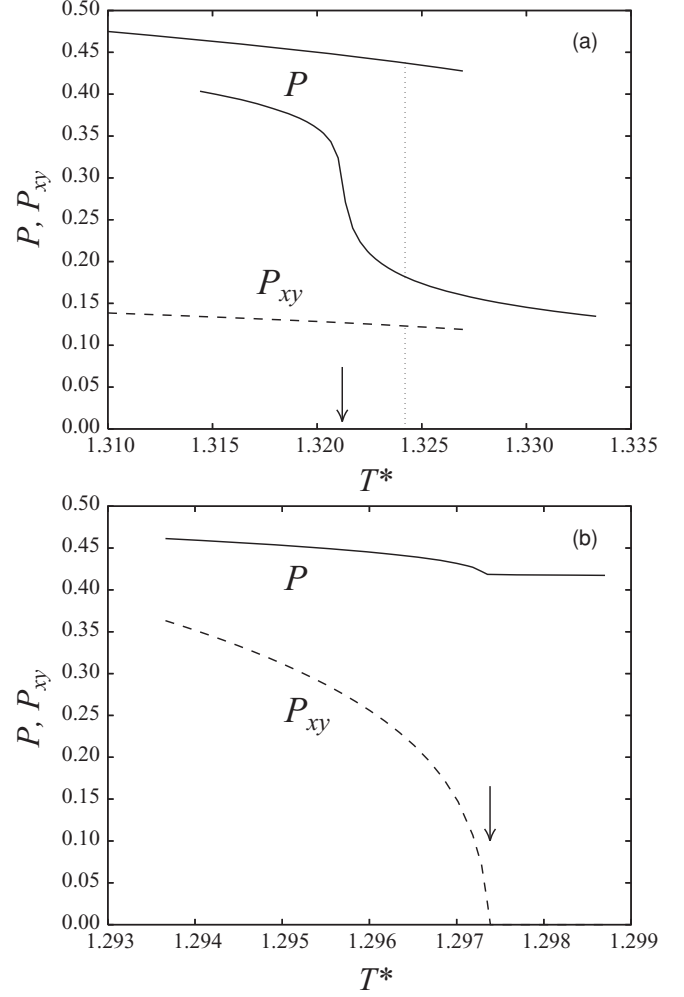


FIG. 14. Order parameters  $P$  and  $P_{xy}$  as a function of reduced temperature  $T^*$  from mean-field theory. (a)  $h = 60$ ; (b)  $h = 5$ . Continuous curves:  $P$ . Dashed curves:  $P_{xy}$ . In (a), vertical dotted lines indicate location of first-order LS phase transition, while arrow points to bulk temperature. In (b), arrow indicates temperature of continuous LS transition.

Now it is not symmetrically located with respect to the two surfaces, but closer to the surface with the weakest coupling constant (i.e., the right surface). This feature can be seen in Figs. 16(c) and 16(d), where the uniaxial order-parameter profile  $P_i$  and director tilt-angle  $\phi_i$  are plotted for the case  $h = 15$  and for the two phases coexisting at the LS transition. For comparison, the corresponding symmetric profiles for the case  $\epsilon_s^{(1)} = \epsilon_s^{(2)} = \epsilon$  are also plotted in panels (a) and (b).

(2) In the second case, the surface couplings are  $(\epsilon_s^{(1)}, \epsilon_s^{(2)}) = (\epsilon, 0.219\epsilon)$ . Here conditions of nematic wetting only prevail at one surface (Appendix A). The shift in the LS transition curve is much more drastic: The maximum is lower, and the curve crosses the bulk transition temperature at a higher value of  $h$  (see Fig. 15). For narrow pores, the profiles now reveal that the step is located next to the weaker surface, as expected [see Figs. 16(e) and 16(f)]. The pore width at which the transition changes from first to second order also moves to higher values (not shown in Fig. 15).

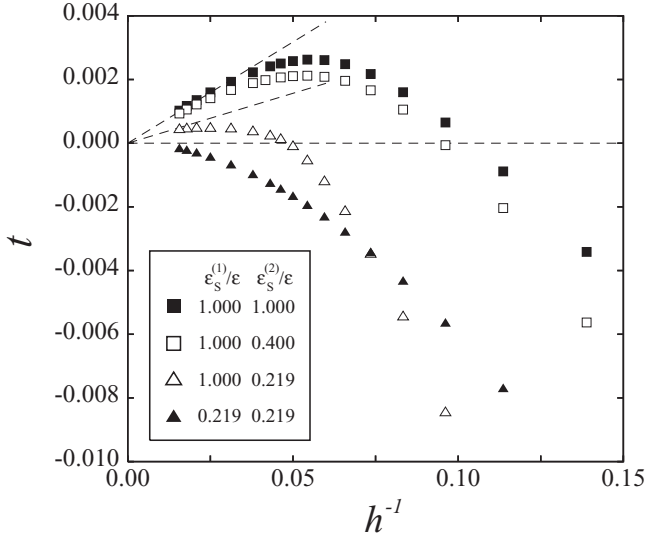


FIG. 15. Phase diagram for the hybrid cell in the  $t-h^{-1}$  plane, with  $t = (T - T_{\text{IN}})/T_{\text{IN}}$ , for different values of the surface couplings  $\epsilon_s^{(1)}$  and  $\epsilon_s^{(2)}$  (indicated in the inset), as obtained from mean-field theory. Dashed lines correspond to the lowest-order Kelvin equation in each case (see text).

(3) Finally, we have examined the case  $(\epsilon_s^{(1)}, \epsilon_s^{(2)}) = (0.219\epsilon, 0.219\epsilon)$ . Now partial wetting applies in both surfaces and, as seen in Fig. 15, the LS transition curve exhibits no maximum. The isotropic film in the slab center is very wide and the two nematic films are not in contact except for very narrow pores. The coexistence profiles for the linear- and step-like phases for a pore of width  $h = 15$  are plotted in Figs. 16(g) and 16(h).

In summary, as the surface coupling of one of the surfaces is made weaker, the step moves toward that surface, and the LS transition temperature shifts to lower values. The cell width where the transition changes from first order to continuous decreases. The maximum in the curve also moves to higher values of pore width, and eventually disappears. This feature is related to the wetting properties of the cell, as shown in the macroscopic analysis of the following section.

#### D. Connection with macroscopic behavior

Much of the behavior shown in the previous sections can be explained using a simple macroscopic approach. For a fluid confined into a pore of width  $h$ , the macroscopic Kelvin equation gives the undercooling (or overheating) of the transition, with respect to the bulk transition, as  $\Delta T(h) = T_c(h) - T_{\text{IN}} = a_1 h^{-1}$ , with  $h \rightarrow \infty$ . As discussed in Appendix B, the coefficient  $a_1$  can be related to the coexistence parameters  $\Delta\gamma$  and  $s_N$  as  $a_1 = \Delta\gamma/s_N$ , where  $s_N$  is the nematic entropy density at the bulk IN transition, and  $\Delta\gamma \equiv \gamma_{\text{SI}}^{(1)} - \gamma_{\text{SN}}^{(1)} + \gamma_{\text{SI}}^{(2)} - \gamma_{\text{SN}}^{(2)}$ , with the superscript denoting the type of substrate, i.e., the left or right substrate (note that the value of the surface tensions does not depend on the preferred surface orientation—as long as the director remains uniform—but only on the value of the surface coupling  $\epsilon_s^{(i)}$ ). For an isolated surface of type  $i$  in contact with a bulk phase, the relation  $-\gamma_{\text{IN}} \leq \gamma_{\text{SI}}^{(i)} - \gamma_{\text{SN}}^{(i)} \leq \gamma_{\text{IN}}$  holds; the right equality corresponds to wetting by nematic, while that in the left pertains to wetting by isotropic. Therefore we may have  $a_1 < 0$  or  $a_1 > 0$ , and the transition curve  $\Delta T(h)$  will monotonically decrease or increase with  $h^{-1}$ , respectively, in the regime of large  $h$ . The sign of  $\Delta\gamma$  depends on the surface couplings: The difference  $\gamma_{\text{SI}}^{(i)} - \gamma_{\text{SN}}^{(i)}$  vanishes for  $\epsilon_s^{(i)} = 0.219\epsilon$ , being

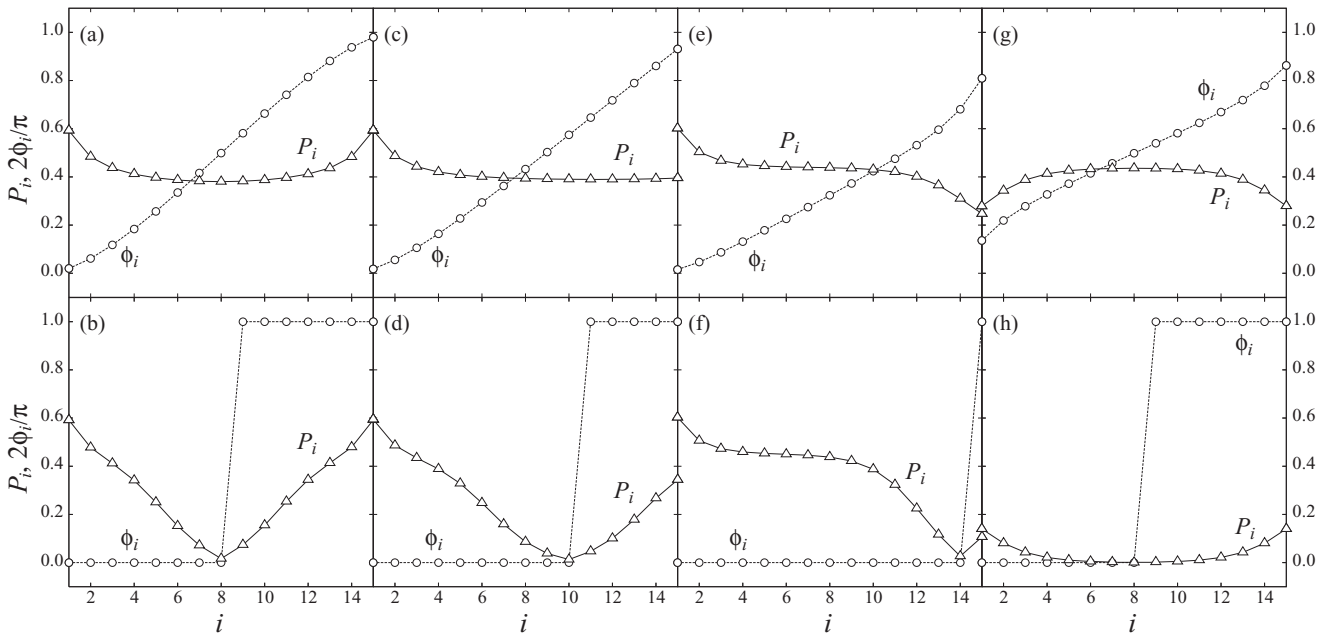


FIG. 16. Order parameter  $P_i$  and director tilt angle  $\phi_i$  for the two phases coexisting at the LS transition for a pore of width  $h = 15$  and different values of the surface coupling constants, as obtained from mean-field theory. Upper panels: Linear-like phase. Lower panels: Step-like phase. The surface parameters  $(\epsilon_s^{(1)}, \epsilon_s^{(2)})$  are as follows: (a) and (b),  $(\epsilon, \epsilon)$ ; (c) and (d),  $(\epsilon, 0.4\epsilon)$ ; (e) and (f),  $(\epsilon, 0.219\epsilon)$ ; and (g) and (h),  $(0.219\epsilon, 0.219\epsilon)$ .

positive (negative) for larger (lower)  $\epsilon_s^{(i)}$ . For the different surface couplings analyzed above, we have

(1)  $(\epsilon_s^{(1)}, \epsilon_s^{(2)}) = (\epsilon, \epsilon)$  and,  $(\epsilon, 0.4\epsilon)$ . Since nematic wetting occurs at both surfaces,  $\gamma_{SI} = \gamma_{SN} + \gamma_{IN}$  (see Appendix A), so that  $\Delta\gamma = 2\gamma_{IN} = 0.0351kTa^{-2}$ . The corresponding  $a_1$  coefficient gives the dashed straight line plotted in Fig. 15; as can be seen, the data follow the behavior predicted by the macroscopic analysis for large  $h$ .

(2)  $(\epsilon_s^{(1)}, \epsilon_s^{(2)}) = (\epsilon, 0.219\epsilon)$ . Now wetting occurs only at one surface. Since  $\gamma_{SI}^{(1)} = \gamma_{SN}^{(1)}$ , we have  $\Delta\gamma = \gamma_{IN} = 0.0176kT$ . Again the MF data follow this behavior in the regime of large  $h$  (Fig. 15).

(3)  $(\epsilon_s^{(1)}, \epsilon_s^{(2)}) = (0.219\epsilon, 0.219\epsilon)$ . Now partial wetting applies and  $\Delta\gamma = 0$ . The LS transition curve departs horizontally from the  $h$  axis and therefore exhibits no maximum, as indeed shown by the MF results in Fig. 15.

As commented above, the MF results indicate that the two surfaces are wet by the nematic phase in the case  $(\epsilon_s^{(1)}, \epsilon_s^{(2)}) = (\epsilon, \epsilon)$ . Whether this is also true in the MC simulations of Sec. IV C is not known, and a more detailed study of the wetting scenario would be necessary. Our present MC data seem to indicate  $a_1 \leq 0$ , which would be incompatible with nematic wetting and even with preferential nematic adsorption, i.e.,  $\gamma_{SN} < \gamma_{SI}$ . However, since the MC profiles indicate that the plates seem to adsorb preferentially the nematic phase, we could still have  $a_1 > 0$  in the real system, but with a change of regime at very large values of  $h$ . Another factor to bear in mind is the presumably large correlation length of the model, associated with the weakness of the bulk transition, which would give rise to slowly decaying interfaces and to the inapplicability of the Kelvin equation except for extremely wide pores.

For smaller separations, the elastic effects in the linear-like phase must be very important, since the director rotates essentially between  $0^\circ$  and  $90^\circ$  in a very short distance. These effects can be shown (Appendix B) to give rise to an additional contribution to the Kelvin equation, namely [4]  $\Delta T(h) = a_1 h^{-1} + a_2 h^{-2}$ , which is the so-called *modified Kelvin equation*. The first term comes from capillary forces, already discussed, whereas the second is due to elastic effects. The elastic contribution is always negative ( $a_2 < 0$ ), promoting capillary isotropization, and dominates the physics in the regime of narrow pores. It explains the decreasing behavior of the LS transition curve for narrow pores. The sign of the first term dominates for very wide pores, and if positive promotes capillary nematization, giving rise to a maximum in the LS transition curve when combined with the second term.

In order to estimate the value of  $a_2$ , it is necessary to compute the elastic constants of the model (Appendix C). As shown in Appendix B,  $a_2 = K\pi^2/8s_N = -1.630a^2\epsilon k^{-1}$ , with  $K$  the model elastic constant. Fig. 10 compares the MF and macroscopic models (note that the comparison can only be made in the regime where the transition is of first order). The overall agreement is not very good. For large  $h$  the surface behavior correctly predicts the capillary LS transition (dashed lines in Fig. 15) but, as soon as the pore becomes narrower, the elastic contribution comes in. However, because the transition is weakly first order, the correlation length, and therefore the interfacial thickness, is very large. Consequently, in the S phase there are thick nematic layers at the walls,

which violate the assumptions of the model. In the other cases studied the agreement is also disappointing, in particular in the partial-wetting cases.

## VI. DISCUSSION

The response of the system to confinement is intimately connected to its wetting behavior. This is especially important in connection with the observation of the step-like structure. In a situation of complete wetting of the two surfaces by the nematic phase, the thickness of the nematic films at temperatures close to the clearing temperature  $T_{IN}$  will be large, and the two films with opposing directors will meet at the slab center when  $h$  is small, producing a step-like phase which will turn into the linear-like phase as temperature is lowered. As the pore gets wider, the step-like phase becomes the isotropic phase with a nematic film adsorbed at each surface. In a partial-wetting situation, the nematic film thickness will be very small, the central isotropic region will be wide, and the two nematic films will never meet, except maybe for very narrow pores.

In light of our simulation results and the interpretation obtained from the MF theory, it is interesting to discuss the quantity  $h_{\max}$  introduced by Chiccoli *et al.*, which these authors obtain from the intersection between their linearly extrapolated data for the transition temperatures and the bulk temperature  $T_{IN}$  (see Fig. 4 in [4]), i.e., the intersection between a linear fit to the triangles in our Fig. 10 and the horizontal line  $T^* = 1.1225$ . Our present MC results indicate that the LS transition curve is below the bulk temperature, at least for the pore widths explored, and that the transition continues as the confined IN transition up to  $h = \infty$ . Therefore, the value  $h_{\max} = 16.6$  obtained by Chiccoli *et al.* from the extrapolated data, and identified as the maximum slab thickness for which the structural phase transition can be found, is somewhat misleading, as it seems to imply that this point terminates a phase transition curve; however, the phase transition continues up to  $h = \infty$ , the step-like phase for narrow pores being smoothly connected (from a thermodynamic viewpoint) with the confined isotropic phase for wider pores and eventually with the bulk isotropic phase for  $h = \infty$ . Our results imply that  $h_{\max}$  obtained by Chiccoli *et al.* does not seem to have any special meaning [12].

## VII. CONCLUSIONS

In this paper we have studied the Lebwohl-Lasher model in a confined slit pore, using MC computer simulation and MF theory. Two types of surface conditions have been imposed, namely symmetric and asymmetric walls, with special emphasis on the latter. The simulations and the data analysis have been carefully performed, with a view to locating accurately the phase transition. For the symmetric walls, we have set a lower limit for the pore width at which the capillary isotropic-nematic transition takes place: The transition is still absent for  $h = 24$ , but the behavior of the heat capacity indicates that it might occur for slightly larger pore widths.

The asymmetric slab was the central target of our investigations and consequently was studied in more detail. A



phase transition, spanning the whole range in pore widths and associated with a change from the linear-like to the step-like director configurations (LS transition), was measured. In all the cases examined,  $1 \leq h \leq 32$ , the transition was found to be continuous. The LS transition involves a structural change of the director configuration but, from examination of the order-parameter profiles, it is evident that the transition corresponds to the IN transition in a confined geometry in a situation where the slab is subject to two conflicting favored directions at the two surfaces. Therefore, there is a single phase transition in the confined slab. These results are supported by a MF theory, which gives qualitatively similar results. Even though the LS or IN transition is continuous in the range  $1 \leq h \leq 32$  according to the simulations, the bulk case,  $h = \infty$ , presents a weakly first-order transition (as obtained from independent simulations). This implies that there must be a change in order at some, probably large, value of  $h$ ; the MF model predicts  $h = 6$  but this value is clearly too small. The case  $h = 1$  has also been examined by MC simulation. Contrary to the transitions in the case  $1 < h \leq 32$ , which belong to the 2D Ising universality class, when  $h = 1$  the transition is essentially different and pertains to the XY-model class.

The case of different surface coupling constants was also analyzed, using only MF theory. The results are qualitatively similar, as long as the nematic phase wets both surfaces. In this case the IN transition can be more clearly identified with the structural transition studied in the literature. When partial wetting applies to one of the surfaces the IN transition occurs between two phases, one of which is the linear-like phase; the other, step-like phase, changes in this case to a phase with a director which is uniform in most of the slab volume. When neither surface is wet, the latter phase consists of a thick central isotropic slab with thin nematic films on the two surfaces.

#### ACKNOWLEDGMENTS

The authors gratefully acknowledge the support from the Dirección General de Investigación Científica y Técnica under Grants Nos. MAT2007-65711-C04-04, MOSAICO, FIS2007-65869-C03-01, FIS2008-05865-C02-02, FIS2010-22047-C05-01, and FIS2010-22047-C05-04, and from the Dirección General de Universidades e Investigación de la Comunidad de Madrid under Grant No. S2009/ESP-1691 and Program MODELICO-CM. R.G.M. would like to acknowledge a research contract from Grant MOSSNOHO.

#### APPENDIX A: SURFACE TENSIONS AND WETTING PROPERTIES

The surface tensions of the three interfaces involved are necessary to discuss the wetting properties of the model and to investigate how the macroscopic behavior is obtained in the confined slab as  $h \rightarrow \infty$ . The isotropic-nematic interface  $\gamma_{IN}$  was computed in slab geometry, by considering a slab of nematic material sandwiched between two isotropic regions at the coexistence temperature  $T^* = 1.3212$ . The uniaxial nematic order-parameter profile is depicted in Fig. 17. The surface tension obtained is  $\gamma_{IN} = 0.0176kT a^{-2}$ . From a fit of the profile to a hyperbolic-tangent function, we get an

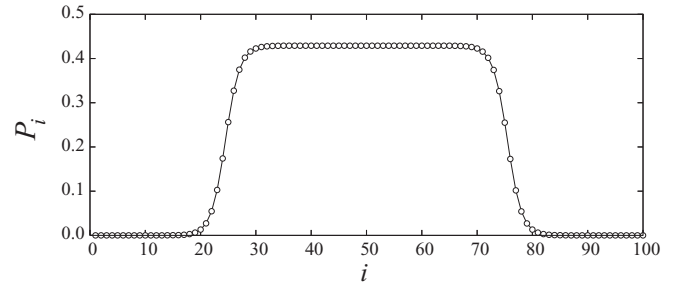


FIG. 17. Order-parameter profile of the isotropic-nematic interface in the MF theory for the Lebwohl-Lasher model.

interfacial width (correlation length) of  $\xi = 2.63a \sim 3a$ . We note that  $\gamma_{IN}$  is relatively small and  $\xi$  relatively large, confirming the weak character of the bulk isotropic-nematic transition.

The plate-isotropic,  $\gamma_{SI}$ , and plate-nematic,  $\gamma_{SN}$ , surface tensions have also been calculated in a range of values of the surface coupling constant  $\epsilon_s$ . Depending on the value of  $\epsilon_s$ , different wetting regimes are obtained. For  $\epsilon_s \leq 0$  there is an infinitely thick isotropic layer adsorbed on the wall, i.e.,  $\gamma_{SN} = \gamma_{SI} + \gamma_{IN}$ , which corresponds to complete wetting of the surface-nematic interface by the isotropic phase (cf. simulations results of Ref. [20]). In the case  $\epsilon_s \gtrsim 0.43\epsilon$  the surface tensions satisfy  $\gamma_{SI} = \gamma_{SN} + \gamma_{IN}$ , implying complete wetting by the nematic phase of the surface-isotropic interface. In the interval  $0 < \epsilon_s \lesssim 0.43\epsilon$  a partial wetting situation arises. Fig. 18 summarizes these results.

Finally, we note that the sign of the surface-tension difference  $\gamma_{SI} - \gamma_{SN}$  depends on  $\epsilon_s$ . It turns out that both  $\gamma_{SN}$  and  $\gamma_{SI}$  decrease with  $\epsilon_s$ , but  $\gamma_{SI} - \gamma_{SN} < 0$  for  $\epsilon_s < 0.219\epsilon$  and  $\gamma_{SI} - \gamma_{SN} > 0$  for  $\epsilon_s > 0.219\epsilon$ . When  $\epsilon_s = 0.219\epsilon$  we have  $\gamma_{SI} - \gamma_{SN} = 0$ ; this case lies of course in the regime of partial wetting (Fig. 18).

#### APPENDIX B: MACROSCOPIC ANALYSIS

In order to understand the behavior of the transition line in the confined system, one can use a macroscopic analysis involving capillary and elastic forces and derive a modified Kelvin equation. This is valid whenever the transition is of first order. The shift in transition temperature  $T(h)$  with respect to the bulk temperature  $T_{IN}$  can be obtained by writing the free energies of the confined isotropic and nematic phases. For a relative temperature  $\Delta T(h) = T(h) - T_{IN}$  but small in

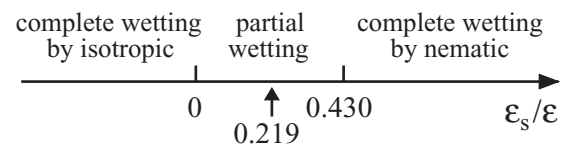


FIG. 18. Wetting regime of the Lebwohl-Lasher model in mean-field theory. For  $\epsilon_s \leq 0$  the substrate is wet by the isotropic phase. For  $\epsilon_s \gtrsim 0.430\epsilon$  the substrate is wet by the nematic phase. In between a partial-wetting regime occurs. The arrow indicates the case where the surface-nematic and surface-isotropic interfaces are equal, which occurs at  $\epsilon_s = 0.219\epsilon$ .

TABLE III. For different values of scaled temperature  $T^*$  or inverse scaled temperature  $\epsilon^* = \epsilon/kT$ , values of uniaxial nematic order parameter  $P$ , scaled elastic constant  $K^*$ , and ratio  $K^*/P^2$  from both MF theory and MC simulation [34]. The highest temperature corresponds to the bulk phase transition in the MF theory.

$T^*$ ( $\epsilon^*$ )	$P$ (sim.)	$P$ (theo.)	$K^*$ (sim.)	$K^*$ (theo.)	$K^*/P^2$ (sim.)	$K^*/P^2$ (theo.)
0.400 (2.500)	0.8922	0.9260	2.5290	2.5726	3.177	3.000
0.750 (1.333)	0.7672	0.8406	1.9747	2.1200	3.355	3.000
0.900 (1.111)	0.7668	0.7901	1.6448	1.8730	3.492	3.000
1.000 (1.000)	0.6863	0.7471	1.3103	1.6745	3.594	3.000
1.080 (0.926)	0.6038	0.7041	0.8587	1.4872	3.693	3.000
1.321 (0.757)		0.4290		0.5520		3.000

absolute value compared to  $T_{IN}$ , we have, for the confined isotropic phase [31]:

$$\frac{F_I}{A} = \gamma_{SI}^{(1)} + \gamma_{SI}^{(2)} + (f_I^{(\text{bulk})} - s_I \Delta T)h + f_s, \quad (\text{B1})$$

where  $f_I^{(\text{bulk})}$  is the bulk free-energy density of the isotropic phase,  $s_I$  the entropy density of the isotropic phase at IN coexistence, and  $f_s(h)$  the free energy per unit area of the step interface.  $f_s(h)$  is only appreciable for small  $h$ , i.e., when the two nematic films are in close contact, and we neglect it here.

Now the nematic phase is assumed to consist of a linearly varying director tilt, with  $\phi = 0$  at one wall and  $\phi = \pi/2$  at the other. Then an elastic contribution  $F_{\text{elas}}$  has to be added:

$$\frac{F_N}{A} = 2\gamma_{SN} + (f_N^{(\text{bulk})} - s_N \Delta T)h + \frac{F_{\text{elas}}}{A}. \quad (\text{B2})$$

At the transition  $F_N = F_I$ . Using  $f_N^{(\text{bulk})} = f_I^{(\text{bulk})}$ , and solving for  $\Delta T$ ,

$$\Delta T = \frac{2(\gamma_{SN} - \gamma_{SI})}{h \Delta s} + \frac{K \pi^2}{8h^2 \Delta s}, \quad (\text{B3})$$

where the elastic energy was written as  $F_{\text{elas}} = AhKq^2/2 = AhK\pi^2/8h^2$ , with  $q = \pi/2h$  and  $\Delta s = s_N - s_I = s_N < 0$  since  $s_I = 0$ . At the transition  $s_N = -0.418ka^{-3}$ . Using reduced units  $h^* = h/a$ ,  $\gamma^* = \gamma a^2/\epsilon$ ,  $T^* = kT/\epsilon$ ,  $s^* = sa^3/k$ ,  $K^* = Ka/\epsilon = 3P^2$  (where  $P = 0.429$  is the nematic order parameter at the transition, see Table III), and  $\gamma_{SN} - \gamma_{SI} = -\gamma_{IN}$  (since we are in a wetting situation),

$$\begin{aligned} \Delta T^* &= -\left(\frac{2\gamma_{IN}^*}{s_N^*}\right) \frac{1}{h^*} + \left(\frac{3\pi^2 P^2}{8s_N^*}\right) \frac{1}{h^{*2}} \\ &= 0.084h^{*-1} - 1.630h^{*-2}. \end{aligned} \quad (\text{B4})$$

The first term comes from capillary forces and promotes capillary nematization, whereas the second is due to the elastic effects and promotes capillary isotropization.

### APPENDIX C: ELASTIC CONSTANT

Since the interaction energy does not couple the relative position of the spins with their orientation, there exists no distinction between the three Frank elastic constants [32] in the Lebwohl-Lasher model, and  $K_1 = K_2 = K_3 \equiv K$ . Priest [33] calculated  $K$  using a molecular-field theory. Here we rederive

the result of Priest in the language of density-functional theory and show numerical results for the bulk elastic constant  $K$ . Cleaver and Allen [34] have obtained the elastic constant by simulation.

We consider a smoothly varying director field corresponding to a distorted director. At each spin site the director unit vector will point along a different direction, and the excess free energy of the bulk, distorted nematic will be

$$\begin{aligned} \frac{F_{\text{ex}}[\{f\}]}{kT} &= -\epsilon^* \sum_{i=1}^N \sum_{j(\text{NN})} \int d\hat{\omega} \\ &\times \int d\hat{\omega}' f(\hat{\omega} \cdot \hat{n}_i) f(\hat{\omega}' \cdot \hat{n}_j) P_2(\hat{\omega} \cdot \hat{\omega}'). \end{aligned} \quad (\text{C1})$$

Here we make explicit the dependence of the distribution function  $f$  on the director. Note that the director need not be the same on each site. Now consider a smoothly varying director field corresponding to a distorted director. We assume that the director rotates about the  $y$  axis by an angle  $\phi$  (see Fig. 1), with a value proportional to the distance of the  $j$ th spin from the  $i$ th spin along the  $z$  axis. Then, assuming  $\phi \ll 1$ ,

$$\begin{aligned} \hat{\omega}' \cdot \hat{n}_j &= \hat{\omega}' \cdot \mathcal{R}_y(\phi) \hat{n}_i = (\omega'_x, \omega'_y, \omega'_z) \cdot (\sin \phi, 0, \cos \phi) \\ &= \omega'_z + \omega'_x \phi - \frac{\omega'_z}{2} \phi^2 + \dots, \end{aligned} \quad (\text{C2})$$

where  $\hat{n}_i = (0, 0, 1)$  and  $\mathcal{R}_y(\phi)$  is a rotation matrix about the  $y$  axis through an angle  $\phi$ . Therefore,

$$\begin{aligned} f(\hat{\omega}' \cdot \hat{n}_j) &= f\left(\omega'_z + \omega'_x \phi - \frac{\omega'_z}{2} \phi^2 + \dots\right) \\ &= f(\omega'_z) + [\omega'_x f'(\omega'_z)] \phi \\ &\quad + \frac{1}{2} [\omega_y'^2 f''(\omega'_z) - \omega'_z f'(\omega'_z)] \phi^2 + \dots \end{aligned} \quad (\text{C3})$$

Introducing (C3) into (C1), subtracting the contribution from the undistorted nematic [which is obtained with  $\hat{n}_i = \hat{n}_j = (0, 0, 1)$ ], noting that the linear term in  $\phi$  vanishes by symmetry and that the ideal free-energy term does not contribute to the difference in free energy between distorted and undistorted fluid, and going to the continuum by using  $a^{-3} \int d\mathbf{r} \rightarrow N$  and  $\phi \rightarrow a \partial_z \phi$ , one arrives at the following expression for the elastic free energy:

$$\begin{aligned} \frac{F_{\text{elas}}[\{f\}]}{kT} &= -\frac{\bar{z}\epsilon^*}{4a} \int_V d\mathbf{r} \int d\hat{\omega} \int d\hat{\omega}' f(\omega_z) \\ &\times [\omega_y'^2 f''(\omega'_z) - \omega'_z f'(\omega'_z)] P_2(\hat{\omega} \cdot \hat{\omega}') [\partial_z \phi(\mathbf{r})]^2. \end{aligned} \quad (\text{C4})$$

$\bar{z}$  is an effective coordination number, which is the number of neighbors of a given one involved in the deformation; since we are rotating about one axis, only 2 of the 6 neighbors in the cubic lattice are involved, so that  $\bar{z} = 2$ . To identify the elastic constant, we use the expression for the Frank elastic energy [32]. Since our distortion is a bend mode, we have, with  $\hat{n} = (\sin \phi, 0, \cos \phi)$  and  $\phi = qz$  (where  $q$  is the wave vector of the distortion),

$$F_{\text{elas}} = \frac{1}{2} \int_V d\mathbf{r} K |\hat{n} \times (\nabla \times \hat{n})|^2 = \frac{1}{2} K V q^2, \quad (\text{C5})$$

where  $V$  is the sample volume. Comparing with (C4), with  $\partial_z \phi = q$ , we arrive at the expression

$$K^* = - \int d\hat{\omega} \int d\hat{\omega}' f(\hat{\omega} \cdot \hat{z}) P_2(\hat{\omega} \cdot \hat{\omega}') \times [(\hat{\omega}' \cdot \hat{y})^2 f''(\hat{\omega}' \cdot \hat{z}) - (\hat{\omega}' \cdot \hat{z}) f'(\hat{\omega}' \cdot \hat{z})]. \quad (\text{C6})$$

$K^* = Ka/\epsilon$  is the scaled elastic constant. This expression is equivalent to the more general one derived by Poniewierski and Stecki [35] in terms of the direct correlation function. To calculate  $K^*$ , we first expand the distribution function using (13) and then use the addition theorem of spherical harmonics, so that

$$\int d\hat{\omega} f(\hat{\omega} \cdot \hat{z}) P_2(\hat{\omega} \cdot \hat{\omega}') = \sqrt{\frac{4\pi}{5}} f_{20} P_2(\hat{\omega}' \cdot \hat{z}). \quad (\text{C7})$$

Therefore the elastic constant is

$$K^* = \left( -\sqrt{\frac{4\pi}{5}} f_{20} \right) \int d\hat{\omega}' [(\hat{\omega}' \cdot \hat{y})^2 f''(\hat{\omega}' \cdot \hat{z}) - (\hat{\omega}' \cdot \hat{z}) f'(\hat{\omega}' \cdot \hat{z})] P_2(\hat{\omega}' \cdot \hat{z}). \quad (\text{C8})$$

Using again the Legendre expansion of the distribution function, taking derivatives, and using a couple of recurrence relations for the Legendre polynomials, the integral over  $\hat{\omega}'$  can be calculated easily, and we obtain the scaled elastic constant:

$$K^* = \left( -\sqrt{\frac{4\pi}{5}} f_{20} \right) \times \left( -3\sqrt{\frac{4\pi}{5}} f_{20} \right) = 3P^2, \quad (\text{C9})$$

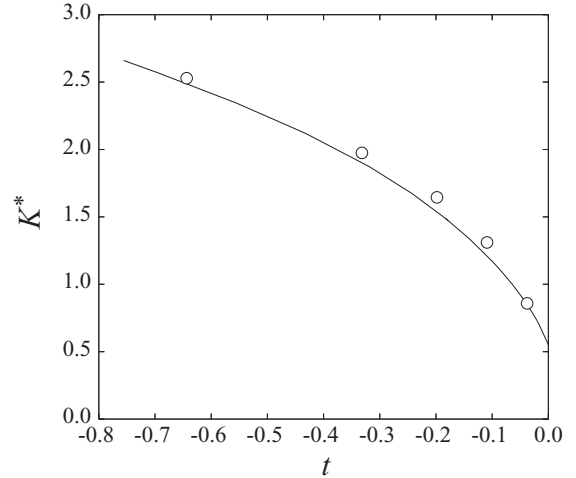


FIG. 19. Scaled elastic constant  $K^* = Ka/\epsilon^*$  for Lebwohl-Lasher model as a function of relative temperature  $t$  (as defined in caption of Fig. 10). Circles: Simulation results of Cleaver and Allen [20]. Continuous curve: Present MF results.

where  $P = \langle P_2(\cos \theta) \rangle$  is the uniaxial nematic order parameter,  $P = \langle P_2(\cos \theta) \rangle = f_{20} \sqrt{4\pi/5}$ . Table III presents a comparison of MF theory with MC simulation. At the highest temperature the MF theory overestimates the elastic constant by almost 75%. The temperature  $T^* = 1.08$  is 3.8% below the transition temperature from the simulation. At the same temperature distance from the MF result ( $T^* = 1.2712$ ) the comparison is quite good:  $K^* = 0.8490$  from theory versus 0.8587 from simulation. In fact, when plotted versus the variable  $t = (T - T_{IN})/T_{IN}$ , the two curves are quite close, see Fig. 19.

- 
- [1] P. A. Lebwohl and G. Lasher, *Phys. Rev. A* **6**, 426 (1972).  
[2] U. Fabbri and C. Zannoni, *Mol. Phys.* **58**, 763 (1986).  
[3] Z. Zhang, O. G. Mouritsen, and M. J. Zuckermann, *Phys. Rev. Lett.* **69**, 2803 (1992).  
[4] C. Chiccoli, P. Pasini, A. Šarlah, C. Zannoni, and S. Žumer, *Phys. Rev. E* **67**, 050703R (2003).  
[5] C. Chiccoli, S. P. Gouripeddi, P. Pasini, R. P. N. Murthy, V. S. S. Sastry, and C. Zannoni, *Mol. Cryst. Liq. Cryst.* **500**, 118 (2009).  
[6] P. Palfy-Muhoray, E. C. Garland, and J. R. Kelly, *Liq. Cryst.* **16**, 713 (1994).  
[7] N. Schopohl and T. J. Sluckin, *Phys. Rev. Lett.* **59**, 2582 (1987).  
[8] H. G. Galabova, N. Kothekar, and D. W. Allender, *Liq. Cryst.* **23**, 803 (1997).  
[9] A. Šarlah and S. Žumer, *Phys. Rev. E* **60**, 1821 (1999).  
[10] F. Bisi, E. C. Gartland Jr., R. Rosso, and E. G. Virga, *Phys. Rev. E* **68**, 021707 (2003).  
[11] B. Zappone, Ph. Richetti, R. Barberi, R. Bartolino, and H. T. Nguyen, *Phys. Rev. E* **71**, 041703 (2005).  
[12] D. de las Heras, L. Mederos, and E. Velasco, *Phys. Rev. E* **79**, 011712 (2009).  
[13] P. I. C. Teixeira, F. Barmes, C. Anquetil-Deck, and D. J. Cleaver, *Phys. Rev. E* **79**, 011709 (2009).  
[14] D. Frenkel and B. Smit, *Understanding Molecular Simulation, From Algorithms to Applications* (Academic Press, New York, 2002).  
[15] H. Kunz and G. Zumbach, *Phys. Rev. B* **46**, 662 (1992).  
[16] N. V. Priezjev and R. A. Pelcovits, *Phys. Rev. E* **63**, 062702 (2001).  
[17] U. Wolff, *Phys. Rev. Lett.* **62**, 361 (1989).  
[18] R. H. Swendsen and J. S. Wang, *Phys. Rev. Lett.* **58**, 86 (1987).  
[19] E. de Miguel, *J. Chem. Phys.* **129**, 214112 (2008).  
[20] D. J. Cleaver and M. P. Allen, *Mol. Phys.* **80**, 253 (1993).  
[21] M. M. Telo da Gama, P. Tarazona, M. P. Allen, and R. Evans, *Mol. Phys.* **71**, 801 (1990).  
[22] M. M. Telo da Gama and P. Tarazona, *Phys. Rev. A* **41**, 1149 (1990).  
[23] P. G. Ferreira and M. M. Telo da Gama, *Physica A* **179**, 179 (1991).  
[24] P. Shukla and T. J. Sluckin, *J. Phys. A* **18**, 93 (1985).  
[25] D. P. Landau and K. Binder, *A Guide to Monte Carlo Simulations in Statistical Physics*, 2nd ed. (Cambridge University Press, Cambridge, 2005).  
[26] J. Salas and A. D. Sokal, *J. Stat. Phys.* **98**, 551 (2000).  
[27] V. Berezinskii, *Sov. Phys. JETP* **34**, 610 (1972).

- [28] J. M. Kosterlitz and D. J. Thouless, *J. Phys. C* **5**, L124 (1972).
- [29] Y. Tomita and Y. Okabe, *Phys. Rev. B* **65**, 184405 (2002).
- [30] N. G. Almaraz, C. Martín, and E. Lomba, *Phys. Rev. E* **82**, 011140 (2010).
- [31] A. Poniewierski and T. J. Sluckin, *Liq. Cryst.* **2**, 281 (1987).
- [32] P. G. de Gennes and J. Prost, *The Physics of Liquid Crystals* (Clarendon Press, Oxford, 1993).
- [33] R. G. Priest, *Mol. Cryst. Liq. Cryst.* **17**, 129 (1972).
- [34] D. J. Cleaver and M. P. Allen, *Phys. Rev. A* **43**, 1918 (1991).
- [35] A. Poniewierski and J. Stecki, *Mol. Phys.* **38**, 1931 (1979).